

Late Quaternary slip rate of the Zihong Shan branch and its implications for strain partitioning along the Haiyuan Fault, northeastern Tibetan Plateau

Wenqian Yao^{1*}, Jing Liu-Zeng^{1,2*}, Yann Klinger³, Zijun Wang¹, Yanxiu Shao¹, Longfei Han¹, Wei Wang², Jinyu Zhang², Zhijun Liu¹

¹ Institute of Surface-Earth System Science, School of Earth System Science, Tianjin University, Tianjin, 300072, China

² State Key Laboratory of Earthquake Dynamics, Institute of Geology, China Earthquake Administration, Beijing 100029, China

³ Université de Paris, Institut de Physique du Globe de Paris, UMR 7154 CNRS, Paris, France

Corresponding author: Wenqian Yao (wenqian_08@163.com), Jing Liu-Zeng (liuzeng@tju.edu.cn)

Key Points:

- The slip rate of the Zihong Shan fault is determined to be 1.9 ± 0.6 mm/yr over the last ~13 ka.
- The minimum total horizontal slip rate across the Hasi Shan section is 4.1 ± 0.6 mm/yr, similar to other sections of the Haiyuan fault.
- The Zihong Shan fault itself could be the source of an earthquake of magnitude $M_w \sim 7$, or larger.

This article has been accepted for publication and undergone full peer review but has not been through the copyediting, typesetting, pagination and proofreading process, which may lead to differences between this version and the [Version of Record](#). Please cite this article as doi: [10.1029/2021JB023162](https://doi.org/10.1029/2021JB023162).

This article is protected by copyright. All rights reserved.

Abstract

Geometrical complexities such as bends and branches are ubiquitous along strike-slip faults. Understanding strain partitioning between the different fault strands along such sections is key to assessing kinematics and evolution through time of a fault system and related seismic hazards. The Haiyuan fault, one of the longest strike-slip faults of the Tibetan Plateau, has developed a multi-stranded complex fault geometry along the Hasi Shan restraining bend. In this study, we quantified the slip rate of the ~50-km-long Zihong Shan fault, which is the poorly-known southernmost fault strand of the Hasi Shan restraining bend. We computed high-resolution DEMs and orthophotos to document the offset landforms along this fault using drone surveys. At selected sites with well-preserved offset geomorphic markers, we quantified displaced terraces and channels using microtopography analysis. We dated the abandonment age of these terraces using ^{10}Be cosmogenic depth profiles and OSL dating techniques. It yields a left-lateral slip rate of 1.9 ± 0.6 mm/yr since ~13 ka, which is similar to the rate of the main Hasi Shan branch that ruptured during the 1920 Haiyuan earthquake. The minimum total horizontal slip rate system summed over the multiple strands of the Haiyuan fault at the Hasi Shan restraining bend is 4.1 ± 0.6 mm/yr, without considering the vertical deformation rate of these fault strands. The rate is thus slightly smaller than, but comparable to, slip-rates determined along the rest of the Haiyuan fault, east and west of the Hasi Shan restraining bend.

Plain Language Summary

Quantifying the slip rate of each fault strand in an area with complex fault geometry is key to understanding how deformation is accommodated along different sections of a large strike-slip fault. Here, studying the poorly-documented left-lateral strike-slip Zihong Shan fault strand provides critical insight into strain partitioning between fault strands along the complex Haiyuan strike-slip fault system. Combining our displacement measurements and geochronology data yields a geological slip rate of 1.9 ± 0.6 mm/yr since ~13 ka along the Zihong Shan fault. The minimum total horizontal slip rate across the entire Hasi Shan restraining bend is thus 4.1 ± 0.6 mm/yr. This value is slightly less, although consistent, than rates obtained farther east and west along the Haiyuan fault. However, the vertical deformation of different strands at the Hasi Shan restraining bend should not be overlooked and could make for the difference. The seismic hazard along the Zihong Shan branch might be greatly underestimated.

1 Introduction

Strike-slip faults often consist of linear segments separated by geometrically complex zones consisting of stepovers, lateral branching, or bends (Sylvester, 1988; Norris & Cooper, 2000; Cunningham & Mann, 2007; Blisniuk et al., 2010; Klinger, 2010). At restraining bends, a fault could branch into multiple subparallel strands with possibly different kinematics that merge at depth to form a complex “flower structure” (Gaudemer et al., 1995; Fuis et al., 2001; Bowman et al., 2003; Dair & Cooke, 2009; Daout et al., 2016a, 2016b; Allen et al., 2017). Along many of the large continental strike-slip fault systems in the world, such as the San Andreas fault, the Alpine fault, the Bulnai fault, or the Dead Sea fault, distributed tectonic deformation over different fault strands can result in complex spatial and temporal patterns of fault interaction (Yule & Sieh, 2003; Bennet et al., 2004; Dair & Cook, 2009; Choi et al., 2018; Zinke et al., 2019) and strain partitioning

(Jones & Wesnousky, 1992; Kendrick et al., 2002; Daëron et al., 2004; Bennet et al., 2004; Dair & Cook, 2009; Onderdonk et al., 2015; Daout et al., 2016a, 2016b; Burgette et al., 2019).

Determining how strain is distributed between multiple parallel faults in a complex strike-slip fault system is critical to understanding variations of fault slip in space and time and, thus, to make a well-informed seismic hazard assessment (e.g., Norris & Cooper, 2000; Thompson et al., 2002; Bennett et al., 2004; Dair & Cooke, 2009; Onderdonk et al., 2015; Choi et al., 2018; Burgette et al., 2019). Slip partitioning involves the distribution of different fractions of the total slip on several faults, possibly with similar net directions (Bowman et al., 2003). For instance, Bennett et al. (2004) pointed out the codependence between faults in a slip partitioning system, that is, change in the rate on one fault is matched by an equal and opposite change in the rate on the other. In some cases, a fault becomes miss-oriented and thus inefficient to accommodate significant slip, leading to the progressive abandonment of that fault to the benefit of other faults of the system (Dair & Cooke, 2009). Therefore, encompassing the entire geometry of a fault system together with a well-constrained fault slip rate for each fault strand of the system is of considerable importance to establish an accurate budget of deformation (Weldon & Sieh, 1985; Dair & Cooke, 2009; Daout et al., 2016b; Burgette et al., 2019; Matrau et al., 2019).

The Haiyuan fault is a major continental strike-slip fault of the northeastern Tibetan Plateau. This fault consists of long straight sections separated by extensional jogs, step overs, and restraining bends of varying width (Figure 1). Near the Hasi Shan (from 104.3°E ~ 104.7°E, Chinese: “Shan” = mountain), the Haiyuan fault broadens to an ~18 km wide zone, which constitutes the most prominent discontinuity along the entire fault. The Haiyuan fault splays into several branches, either strike-slip, thrust, or both. From south to north, the fault system consists of the Zihong Shan fault, the Hasi Shan frontal fault, the Liushashui fault, and the Shuanglong fault (Figure 2). Previous studies have mainly focused on the Hasi Shan frontal fault, as it is the branch that ruptured during the 1920 Haiyuan M_w 7.9 earthquake (IGCEA & NBCEA, 1990; Zhang et al., 2005; Li et al., 2009; Ren et al., 2015; Matrau et al., 2019; Ou et al., 2020). In comparison, little is known about the other three branches. The Zihong Shan fault, in particular, naturally linking to the Laohu Shan section at ~104.08°E, shows a ~50-km linear trace with clear geomorphic evidence of displaced Quaternary landforms (Figure S1); quantifying the slip rate for this fault is thus important to better understand the degree of slip partitioning, kinematics, and earthquake recurrence within the Haiyuan fault system.

Figure 1.

In this work, we quantify the slip rate of the Zihong Shan fault using displaced terraces as deformation markers. We measure offsets of terraces and channels at three sites with well-preserved offset landforms, taking full advantage of high-resolution digital elevation models (DEMs) and orthomosaic photos derived from small uncrewed aerial vehicle (sUAV) photography. By combining offset values with dating by cosmogenic exposure age and optically stimulated luminescence, we bracket the average late Quaternary slip rate for the fault. We also infer coseismic offsets through statistical analysis of displacement measurements of geomorphic features along the fault. Finally, we explore the role of the Zihong Shan fault in strain partitioning in the framework of the multi-stranded section of the Haiyuan fault system and its significance for seismic hazards.

2 Background

The ~1000 km-long left-lateral Haiyuan fault is a major active fault of the northeastern Tibetan Plateau and one of the longest active faults in Tibet. This fault, together with the Altyn Tagh, Kunlun, and Xianshuihe faults, accommodates a significant part of the eastward extrusion of the Tibetan Plateau relative to the Gobi-Ala Shan platform to the north, in response to the Indian-Eurasian collision (Figure 1) (e.g., Tapponnier & Molnar, 1976; Burchfiel et al., 1991; Avouac & Tapponnier, 1993; Tapponnier et al., 2001). The Haiyuan fault branches off the Altyn Tagh fault in the Qilian Shan Range and runs from Hala Hu (~97°E) within the central Qilian Shan with N110°E azimuth. Continuing eastward and veering to strike N140°E east of the Yellow River (~104°E), the fault eventually changes to an approximately north-south azimuth along the Liupan Shan (east of 106°E). Then, it resumes to an azimuth N100°E before merging with the northern boundary of the Qinling Shan (Gaudemer et al., 1995). Near 102.3°E, the Gulang-Zhongwei fault branches off the Haiyuan fault and extends for another ~300 km in an E-W direction. To the east of the junction, strain is partitioned between the Haiyuan and Gulang-Zhongwei faults (Gaudemer et al., 1995; Daout et al., 2016a). After crossing the Yellow River, the Gulang-Zhongwei fault swerves into a nearly north-south strike for another ~100 km to reconnect with the main Haiyuan fault near Guyuan. Thus, the Gulang-Zhongwei fault is a major branch of the Haiyuan fault system at the regional scale. As the azimuth of the fault changes from nearly east-west to north-south, the kinematics of which also gradually changes, from left-lateral strike-slip in the west to thrust motion and folding in the east (Gaudemer et al., 1995; Chai et al., 2003; Li et al., 2019).

Both the Haiyuan and Gulang-Zhongwei faults have produced large historical earthquakes. The 1709 Zhongwei M 7.5 earthquake ruptured most central and the part east of the Gulang-Zhongwei fault (Min et al., 2001; Li et al., 2019). The 1920 Haiyuan M_w 7.9 earthquake produced an ~220-km-long rupture along the Haiyuan fault with a maximum slip of ~10 m (Deng et al., 1986), although other studies have suggested smaller maximum and average coseismic offsets (Ren et al., 2015; Ou et al., 2020). During the 1927 Gulang M 8.0 earthquake, both the Haiyuan fault and part of the Gulang fault ruptured, making the event might be an additional example of coseismic slip partitioning with a coseismic sinistral offset of approximately 2.4–7.5 m along the 120-km-long Lenglongling section of the Haiyuan fault (Guo et al., 2020).

The Haiyuan fault is generally segmented into seven sections, named from west to east: Hala Hu (HLH), Lenglong Ling (LLL), Jinqiang He (JQH), Maomao Shan (MMS), Laohu Shan (LHS), Haiyuan fault (HYF, in the narrow sense), and Liupan Shan (LPS) sections (Figure 1). They are separated by geometric complexities of varying sizes, such as pull-apart basins, restraining bends, and fault branching. Among them, the Hasi Shan restraining bend, which is located to the west of the HYF, is the largest geometric complexity. There, the Haiyuan fault splits into four strands bounding the Hasi Shan and Mijia Shan. The most prominent strand (Hasi Shan frontal fault) runs along the southern front of the Hasi Shan that peaks at 2987 m (Figure 2). To the south, the ~50-km-long Zihong Shan fault cuts through alluvial fans that are fed by drainages originating from the Hasi Shan. To the north, the Liushashui fault cuts through the middle of the mountain range, whereas the Shuanglong fault bounds the Hasi Shan to the north. Farther east, the Hasi Shan frontal fault and the Zihong Shan fault bend northward through the Huangliang Tan pull-apart basin (IGCEA & NBCEA, 1990; Li et al., 2009) and eventually merge with the Liushashui and Shuanglong faults (Figure 2b). Among these four strands, previous studies primarily focused on the Hasi Shan frontal fault, which ruptured during the 1920 Haiyuan M_w 7.9 earthquake (IGCEA & NBCEA, 1990; Deng et al., 1986; Zhang et al., 2005; Li et al., 2009; Ren

et al., 2015; Matrau et al., 2019; Ou et al., 2020). The Zihong Shan fault, however, remains poorly known; It was qualitatively recognized as a reactivated strike-slip fault from an old reverse fault (Tian et al., 2000), and it has been suggested that it accommodates a limited fraction of the deformation of the Haiyuan fault (Matrau et al., 2019). However, satellite images show clear geomorphic evidence of offset Quaternary landforms along the Zihong Shan fault (Figure S1), which would suggest more significant Quaternary activity than previously proposed.

Figure 2.

Prior studies along the Haiyuan fault have provided an extensive range of slip rates, from 2.3 to 24 mm/yr (e.g., Burchfiel et al., 1991; Liu et al., 1992; He et al., 1994; Gaudemer et al., 1995; Yuan et al., 1998; Zhang et al., 1988; Lasserre et al., 1999, 2002; Li et al., 2009). The most recent reevaluation of geologic slip rates using high-resolution DEMs and new geochronological dating results point towards a first-order agreement with geodetic slip rates (Cavalié et al., 2008; Jolivet et al., 2013; Daout et al., 2016a; Zheng et al., 2017; Jiang et al., 2017; Yao et al., 2019; Shao et al., 2021). Near the Hasi Shan, Matrau et al. (2019) bracketed the average slip rate of 2.7 ± 0.5 mm/yr since ~50 ka along the Hasi Shan frontal strand alone, which is indeed lower than the reported slip rate of 4–10 mm/yr to the east and the west (Zhang et al., 1988; Li et al., 2009; Yao et al., 2019). Hence, it is important to accurately assess the slip rates along the other parallel fault strands in the multi-stranded Hasi Shan section.

3 Materials and Methods

To derive an accurate slip rate of the Zihong Shan fault, we used a combination of high-resolution DEMs, orthomosaic photos, and new geochronological dates.

3.1 High-resolution Topographic Data Processing

To constrain the average slip rate on the fault, obtaining precise displacement is a key prerequisite. First, combining satellite imagery and field observations, we mapped the fault geometry and identified displaced morphology along the fault. Then, we used a small uncrewed aerial vehicle (sUAV) to survey offset landforms at selected sites and processed imagery in three steps: 1) We collected aerial images with an average overlap of 75% straddling the fault trace and covering an area of ~11.2 km². 2) Using structure-from-motion (SfM) techniques, these photographs were processed to produce digital elevation models (DEMs) and orthomosaic photos with a centimeter ground resolution. 3) We then utilized ArcGIS to derive hillshade, slope, and contour plots with high-resolution DEMs and to extract swath topographic profiles perpendicular and parallel to the fault trace.

3.2 Offset Measurements

We first outlined the fault trace and identified well-preserved displaced geomorphic markers (such as channels, ridges, and risers) based on high-resolution orthomosaic photos and DEMs. We chose the sites of Shimen and Dougouping for a detailed investigation of geomorphic mapping and measuring offsets, as they show well-preserved geomorphic markers (fans, terraces, and channels) with different offsets (Figures 2, 3, and 4). We mapped these markers from the high-resolution DEMs and measured offsets by matching piercing lines corresponding to the same

marker on each side of the fault. Multiple approaches can be used to measure offsets, such as a manual back-slipping approach (a couple of examples, [Klinger et al., 2011](#); [Manighetti et al., 2015](#)) or computer-based semi-automatical tools ([Zielke and Arrowsmith, 2012](#); [Haddon et al., 2016](#); [Stewart et al., 2018](#)). The manual back-slipping approach determines the lateral offset through visual reconstruction of the original geometry of these displaced landforms. In this approach, the projected point of each piercing line was determined by the intersection between the far- and near-trend of the fan edge, terrace riser, or thalweg of a channel and the mapped fault trace. Hence, manual back-slipping contains a degree of subjectivity, and its quality might be rather dependent on the past experience of the operator. In the last decade, several semi-automatical tools have been developed to assist in measuring geomorphic offsets while trying to mitigate the issues related to manual measurement ([Zielke and Arrowsmith, 2012](#); [Haddon et al., 2016](#); [Stewart et al., 2018](#)). Nonetheless, a comparison of offsets measurements performed by manual and semi-automatic back-slipping approaches show that the two ways are in general consistent with each other within uncertainties (e.g., [Zielke and Arrowsmith, 2012](#); [Manighetti et al., 2015](#)).

Here, we adopted the Matlab tool, “LaDiCaoz_v2” of [Haddon et al. \(2015\)](#). The LaDiCaoz_v2 cross-correlates a “representative” topographic profile taken across the potential offset landform and parallel to the fault direction its counterpart on the other side of the fault. Based on the value of the cross-correlation of topographic data on either side of the fault, which ranges from -1 to 1, the code calculates the range of surface offset. The optimal offset is determined for the maximum value of the cross-correlation coefficient. During the last step, the user determines uncertainty limits based on the cross-correlation curve, generally equal to a $1\sigma\sim 2\sigma$ standard deviation for a Gaussian probability density function. Depending on the morphology of the displaced marker (e.g., sharpness, sinuosity, and size), degree of modification, and angle between the piercing lines and the fault, we assigned a qualitative rating to each offset from fair, to good, to poor ([Figure S2](#)). A fair offset represents the well-preserved displaced markers on both sides of the fault showing high sharpness, low sinuosity, and a high angle of intersection with the fault. A good offset refers to markers with a moderate sinuosity of the linear features and markers that exhibit a moderate angle of intersection with the fault. Offset markers rated as poorly recognized offset markers (low quality) denote high sinuosity and/or a low angle to the fault. Eventually, the cumulative offset probability density (COPD) is computed to analyze the offset distribution along the fault for all measured left-lateral horizontal offsets.

In total, based on measurements realized with the semi-automatical tool, LaDiCaoz_v2, anywhere we had the relevant DEM data, complemented by a few manual measurements at the Dougou Ping site, we measured 73 individual horizontal and vertical offsets for displaced geomorphic markers, and we determined their associated uncertainties along the fault.

3.3 Geochronological Methods

We sampled different sites selected for slip rate determination. Dating techniques included optically stimulated luminescence (OSL) and in-situ cosmogenic nuclide (^{10}Be). OSL samples were collected and kept away from light in stainless steel tubes 5 cm in diameter and 30 cm in length. OSL samples were processed and measured under subdued red laboratory light at the State Key Laboratory of Earthquake Dynamics, China Earthquake Administration, following the sample treatment methods described in [Yang et al. \(2018\)](#). Concerning the use of cosmogenic radionuclide (CRN) exposure dating (e.g., [Van der Woerd et al., 1998](#); [Gosse & Phillips, 2001](#); [Hidy et al., 2010](#); [Yao et al., 2019](#); [Matrau et al., 2019](#); [Shao et al., 2021](#)), we favored a depth profile strategy.

This strategy allows mitigating some of the main issues related to surface samples such as the inheritance, sediment redeposition, or post-abandonment surface modification (Anderson et al., 1996; Van der Woerd et al., 1998; Gosse & Phillips, 2001; Hidy et al., 2010). For the depth profile approach, samples of quartz-rich sand were collected at different depths in a ~2 m deep pit excavated into the flat patch of each terrace of interest. Four to five ~2 kg sandy sediments were collected in each pit from a 10 cm-wide swath at different depth intervals from top to bottom. Then, samples were sieved in the field to remove the coarse grains (> 2 mm) (Hidy et al., 2010). All ¹⁰Be cosmogenic nuclide samples were preprocessed following standard chemical procedures and packed into targets at the Surface Processes Laboratory at Arizona State University and Tianjin University. Accelerator mass spectrometry (AMS) measurements of the final targets were conducted at the Prime Lab at Purdue University and Tianjin University.

4 Observations and Results

Two sites were selected for surveying and detailed mapping: Shimen (SM) to the west and Dougouping (DGP) to the east (Figure 2b). The Shimen site is characterized by alluvial fans, whereas the Dougouping site maintains well-preserved terraces and channels. In addition, we conducted systematic horizontal offset measurements, using both manual back-slipping and LaDiCaoz_v2 tool, for displaced geomorphic markers along the section east of Dougouping. Combining all the other offset values collected by automatic measurements beyond the Dougouping site, we analyzed the average coseismic offset along the fault.

4.1 Shimen site

The Shimen site is located along the western part of the Zihong Shan fault and to the west of the Yellow River. There the fault cuts through the apron of coalescent alluvial fans originating from the Mijia Shan (Figures 2b and 3). The current active channel R1 flows down the Mijia Shan and cuts into steeply dipping orange-yellow Neogene sandstone beds. A narrow light gray Quaternary complex fan is sandwiched between remnants of the Neogene beds. Five generations of alluvial fans can be distinguished with distinctive heights above the active streambed. These fans are named f5, f4, f3, f2, and f1, from higher to lower relative elevations. Fan f3 is preserved on both sides of the fault, whereas the other four fans are all remnants preserved only on one side of the fault. Similar to alluvial fans developed at the southern front of the Hasi Shan range (Matrau et al., 2019), the spatial distribution of these alluvial fans is likely controlled by the underlying Neogene bedrock. For example, the southern fan f3, inset between remnants of Neogene bedrocks, is narrower than its northern counterpart. The linear fault trace cuts through fan f3, forming a 4.8 m-high scarp (Figure 3d, 3e, and 3f). The well-preserved fan f3 also records a cumulative horizontal left-lateral offset: Reconstruction of the original fan geometry by realigning near- and far-field projection of the eastern edge of the f3 surface across the fault trace suggests an average horizontal offset of 47.6 ± 5.8 m (AA' and aA', Figure 3b, 3g and 3h).

Figure 3.

4.2 Dougouping Site

The Dougouping site is located in the middle portion of the Zihong Shan fault (Figure 2b). At this location, gray Quaternary alluvial fans that unconformably overly the reddish Neogene beds formed a bajada at the toe of the Hasi Shan Range that have later been partially dissected by active channels flowing into the Yellow River. According to large-scale geomorphic mapping by Matrau et al. (2019), the Dougouping site is located on top of the most recent terrace, T1, that extends continuously from their site 1 located at the base of the Hasi Shan Range. In this study, we refined their mapping of the alluvial fan complex that extends ~5.3 km to the Dougouping site. We recognized several channels (e.g., R2, R3, R4, R5, C3, C4, and C5) that incise the fan complex surface and form a series of distinct inset terraces. Flights of terraces and incising channels are evidently displaced by the repeated activity of the Zihong Shan fault.

The Zihong Shan fault trace is distinctively visible on 0.4 m-resolution aerial photos (Figure S3). The fault is expressed as a quasi-linear feature with a >1 m-high scarp cutting through landforms. Nicely displaced geomorphic markers are well preserved (Figure 4). To the east, an ephemeral channel, R2, with a maximum width of ~188 m originates from the Hasi Shan, crosses the Zihong Shan fault, and joins channel R3 at the southern tip of the terrace surfaces. To the west, channel R5 has a relatively uniform width of ~70 m. Unlike the other three rivers, channel R4 is a short local modern channel originating ~200 m to the north of the fault. Below, we describe separately the tectonic-geomorphic evidence, as well as our offset determination, at the Dougouping site for the sections to the east and west of channel R3.

Figure 4.

The section to the east of channel R3

Between R2 and R3, five primary levels of the terrace can be distinguished, including T0, T1, T2, T3, and T4, from low to high. In addition, four minor terraces, T0', T2', T3', and T4', can also be recognized and are still mappable on both sides of the Zihong Shan Fault (Figure 5 and Figure S1). All terrace surfaces are essentially smooth and paved with a mixture of gravels, cobbles, and sporadic boulders. As shown by topographic profile N1 to the north, parallel to the fault, the terrace treads sandwiched between R2 and R3 are separated by 0.5 m- to 6.8 m-high risers. T0 is immediately located 4.7 m above the R3 streambed. The surface T1 has a droplet shape to the north of the fault while it consists of an elongated strip to the south, approximately 6.8 m above T0. The T1/T0 riser seems to be artificially modified to the north of the fault because of extremely steep scarp of the riser base. Additionally, the manmade water tank on the T0 tread takes advantage of the natural spring at the fault. Whereas to the south, the T1/T0 riser disappears immediately after crossing the fault, T1 is therefore almost directly standing above the R3 riverbed on the southern side. Standing ~3.9 m above T1, T2 is located from the right (west) bank of C4 and is preserved as an elongated strip to the north of the fault. It extends ~50 m to the south of the fault. T2' is preserved as a set of sporadic surfaces both to the north and south of the fault. The highest and best-preserved terrace, T4, appears as a flat strip. One sublevel can be recognized to the north of the fault as T4', which is located 0.5 m below the western edge of T4. The riser T4'/T2' is 2.8 m high and it exhibits a degraded slope. To the east of C5, T3 and T3' are preserved on both the north and south sides of the fault. The T3/T3' riser extends clearly ~50 m to the north of the fault. To the south of the fault, it becomes obscured by rills and manmade barriers. A 1.9 m high

scarp is documented from the extracted topographic profile perpendicular to the fault, which is visible as well as from the field section located at the western edge of R2 (Figure 5d). In this section, the fault cuts through the Neogene sandstones and thrusts them on the top of the upper Quaternary conglomerates that have accumulated in the broad foreland bajada of the Hasi Shan. This indicates a reverse component in addition to the strike-slip component.

Based on detailed mapping of landforms, several piercing lines can be identified across the Zihong Shan Fault. On both sides of the fault, the eastern edge of T4, crest and base of the T4/T2' and T3/T3' risers, and the riverbed of C4 and C5, are all linear and well defined (Figure 5e and 5f). Indeed, some curvature is still found when these linear markers get closer to the fault, which is factored in our measurement uncertainties. For instance, C4 and C5 show left-lateral offsets with dog-legged shapes when they cross the fault. We cannot rule out the possibility that the portion of this dog-legged shape might have resulted from original meandering, and it needs to be considered during the displacement measurements.

We determined the displacement of C5 to be 12.1 ± 3.6 m. Realignment of C4 documents a slightly larger offset of 21.9 ± 5.1 m (EE' and BB', Figure 5f). We also measured an offset of 20.5 ± 4.5 m by matching the T2 surface located on the right bank of C4, which is consistent with the displacement of C4. Along the east bank of C4, since T4' was formed by the incision of T4 and is only preserved upstream of the fault, we acquired displacements by aligning the base and crest of the T4'/T2' riser with the T4/T2' riser, their downstream counterparts. It yielded two offsets of 17.6 ± 2.8 m and 24.1 ± 3.2 m, respectively (cc' and CC', Figure 5f). Although the eastern edge of the T4 tread to the north of the fault is hardly distinguishable near the fault, which results in additional uncertainties in the offset measurements, the piercing line of the edge on each side is fairly straight. We therefore assumed local erosion to explain that the northern riser is fading away and we projected the well-defined straight edge into the fault. By considering the far-field and near-field piercing lines to the north of the fault, we acquired an average offset of 12.6 ± 2.6 m (DD', Figure 5f). Farther to the east, for the T3/T3' riser, although its northern part exhibits a clear base and crest, local erosion when one is approaching the fault, induces uncertainties in the displacement measurements. By utilizing 0.5 m contour lines, we then projected the T3/T3' riser into the fault and we determined a base and a crest offset of 16.2 ± 3.1 m and 19.5 ± 1.1 m, respectively (FF' and GG', Figure 5f). We also pay attention to the east edge of the T3 tread, which shows a horizontal displacement. Assuming that the curve of the downstream edge when one is approaching the fault might have resulted from lateral erosion, as it is located in the way of R2, our offset measurement of the edge should be considered as a minimum value. We thus determined horizontal offsets of 12.1 ± 4.2 m (HH', Figure 5f). In addition, we observed an apparent vertical offset from the eastern wall of T3 cut by R2, demonstrating SW-directed thrusting of the Zihong Shan fault (Figure 5d). On the other hand, the sinistral slip of R3 is found to the west with a curve westward to the south of the fault, which contributed to the uncertainty when the offset was determined. Our measurement of the displaced R3 yielded an offset of 45.9 ± 18 m by matching the thalwegs upstream and downstream of R3 (AA', Figure 5e). As a way to benchmark our manual measurements, we also measured similar offsets features by utilizing LaDiCaoz_v2. The corresponding lateral offsets of each aforementioned displaced landforms are 23.4 ± 1.0 m for C4 (BB'), 11.5 ± 1.5 m for C5 (EE'), $20.6^{+8.0/-4.6}$ and $22.4^{+6.8/-4.5}$ m for the base and crest of T4'/T2' riser (cc' and CC'), $16.8^{+5.7/-2.2}$ and $19.1^{+3.5/-3.0}$ m for the base and crest of T3/T3' riser (FF' and GG'), $12.4^{+1.0/-2.4}$ of the east edge of the T3 tread (HH')(Figures S4-S10). Thus, it shows that careful manual measurements, when the morphology is well understood, yields measurements consistent with a semi-automatic approach, although our manual measurements might have larger

uncertainties. Additionally, using LaDiCaoz_v2, we could estimate the vertical offsets of the T3/T3' riser base and the eastern edge of T3 to be respectively $2.3^{+0.1/-0.2}$ m and 2.0 ± 0.2 m (Figures S9 and S10).

Figure 5.

The section to the west of channel R3

The western section is located between R3 and R5 (Figures 4 and 6). Similar to the eastern section, this section includes well-preserved offset terraces and channels. We interpreted six main terraces similar to the eastern part by combining field mapping, 0.5 m contour lines, slopeshade, and one topographic profile that parallels the fault to the north (Figure 6). Our mapping also included three lower additional subterraces, including T_w1' of T_w1 , T_w2' of T_w2 , and T_w4' of T_w4 . Four smooth and shallow channels (C6, C7, C8, and C9) are inset immediately into the base of the T_w4'/T_w2 , T_w5/T_w4' , and T_w4/T_w2 risers, respectively. Unlike channels documented along the eastern section, the upstream part of these channels systematically curves eastward when approaching the fault, which introduces more uncertainties into the offset measurements. We used the straight far-field riverbed of each channel along both the upstream and downstream sections as piercing lines to define offsets. Therefore, matching upstream and downstream parts for C6, C7, and C8 yielded offsets of 14.4 ± 1 m, 30.0 ± 2.1 m, and 14.1 ± 0.7 m, respectively (MM', LM' and II', Figure 6e). A narrow active river, defined as R4, has strong sinuosity and incises deeply between T_w1 and T_w2 , 13.3 m below T_w2 . Most terraces preserved to the north of the fault exhibit a narrow bench and are separated by low and gentle risers. Our measurements utilizing the west and east edges of the T_w5 and T_w2'/T_w2 risers document offsets of 13.5 ± 2.4 m, 20.3 ± 3.5 m and 16.8 ± 3.6 m, respectively (JJ', KK', and NN', Figure 6e). We also used the LaDiCaoz_v2 tool to better constrain these measurements and the automatic calculated left-lateral offsets of channels are $15.4^{+1.6/-2.4}$ m for C6 (MM'), $32.4^{+1.6/-2.4}$ m for C7 (LM'), $14.2^{+1.2/-1.0}$ m for C8 (II') (Figures S11-S13).

Figure 6.

4.3 Distribution of Displacements Along the Fault

Along the fault east of the Dougouping site, many offset channels, terrace treads, and ridges are well preserved, allowing for documentation of cumulative offsets.

For instance, east of the Dougouping site, the Zihong Shan fault runs ~1 km southeastward through the front of some residual topography and crosses several strips of fan surfaces at the Yaoshui Gou site (Figure 2). This site is characterized by numerous offset channels and ridges and a discontinuous left-stepping fault trace with several oblique short normal faults branching northward (Figure 7). We thus systematically identified and mapped displaced small stream channels, terrace treads, and ridges based on sUAV-derived high-resolution orthomosaic photos and DEMs together with field investigations. Combining the measured offsets to the Dougou Ping site, eventually, we obtained a total of 73 displacements, both horizontal and vertical, along the Zihong Shan fault (Table S1, which contains feature ID, geographic coordinates, distance along the fault, optimal, minimum, and maximum horizontal and vertical offsets, uncertainties, feature

type, and measurement rating). **Supporting information Data Set_S1** shows the original and the reconstructed topographies and the corresponding cross-correlation curves for each site. The 73 offset measurements are distributed between $2.1^{+1.4}/_{-1.6}$ m and $29.8^{+2.2}/_{-3.8}$ m (**Figure 8 and Table S1**). The corresponding cumulative offset probability densities (COPDs), which highlight distinct peaks of lateral offset related to individual earthquake events, have been used to infer offset recurrence characteristics, are shown in Figure 8c (Zielke et al., 2010; Klinger et al., 2011). The COPD plot shows that the most prominent peak is at 3.9 m, which indicates the most precise value within the total collected data (Manighetti et al., 2015). A secondary, subtle peak is found at 6.9 m, arguably separable from the prominent peak. A third peak of lower amplitude is suggested at 12.5 m (**Figure 8c**).

Figure 7.

Figure 8.

4.4 Age Determination of the Terraces at the Dougouping Site

We sampled for dating some of the well-preserved terraces (T2', T3 and T4) at Dougouping. As mentioned above, all terraces at the site were mapped as a subset of terrace T1 at Site 1 in Matrau et al. (2019). Following this work, all terraces preserved at the Dougouping site are considered to have experienced negligible erosion and postdeposition modification and to be only affected by regressive channels. All terraces at Dougouping are free of overlying loess deposits that would cause bias for the exposure age. Therefore, we modeled the ^{10}Be concentration and calculated exposure ages for three depth profiles, assuming limited erosion and no shielding effect.

Hereafter, all terraces are named according to the detailed mapping presented in the above sections. To acquire the exposure age of T4, we hand-excavated a ~2 m deep pit in the T4 tread on the upstream side of the fault (**Figure 5f**). The pit was dug where the terrace surface is smooth and leveled. As visible on the high-resolution photographs (**Figure 9a**) and recorded in detailed stratigraphic observations, the sampled section consists of a continuous deposit of massive, angular sandy/cobbly gravel interbedded with a sand lens. One OSL sample collected from the sand lens yielded an age of 13.5 ± 1.1 ka, which represents the age of the depositional phase of terrace T4 before the abandonment of the terrace (**Table 1**). To better constrain the age of abandonment of the terrace, we also collected four sand samples in this pit and modeled the ^{10}Be concentrations with depth following Shao et al. (2021). ^{10}Be concentrations decrease exponentially with depth and yield an exposure age of $13.0^{+0.8}/_{-0.2}$ ka. One sample (170717-02-100) is slightly off from our best-modeled curve for reasons that remain unclear to us. Our best model age from ^{10}Be is consistent with the OSL data that is slightly older than the ^{10}Be model age (**Table 2**). This tendency is consistent with the terrace deposition history since this OSL sample is buried in the terrace; thus, it is reasonable to accept $13.0^{+0.8}/_{-0.2}$ ka as the abandonment age of terrace T4.

We also excavated a 2 m deep pit in terrace T3 tread upstream from the fault to constrain its exposure age. Deposits in this pit are mainly characterized by poorly sorted angular pebbly to bouldery gravel (**Figure 9b**). Near the bottom of the pit, at a depth of 130 cm, a ~30 cm-thick sandy

lens occurs between boulders where we collected one sand sample for OSL dating. It yielded an age of 18.9 ± 2.3 ka (Table 1). Five ^{10}Be sand samples were collected to model a depth profile. Our modeling of these five ^{10}Be samples suggests that the T3 terrace surface was probably abandoned at $11.1^{+0.4}/_{-0.5}$ ka. There exists an ~8000-year gap between the OSL date and the surface exposure age. It is possible that the OSL sample was partially bleached prior to deposition, which is common in alluvial settings (Lian & Roberts, 2006; Rhodes, 2011; Thompson et al., 2018); thus, the OSL dates overestimate the depositional age of the terrace (Table 2).

On the terrace T2' surface, we excavated a pit downstream from the fault. The stratigraphy in this pit can be divided into two layers: a ~30 cm-thick upper layer of poorly sorted and angular gravel and an underlying layer of moderately sorted subrounded gravel with cobbles (Figure 9c). We collected one sample (T2'S-00) in the upper layer and four samples below. In this section, no evidence shows any hiatus between the upper and lower layers. As this pit is close to the fault, we interpret the upper ~30 cm layer to be colluvium that collapsed from the fault scarp located immediately to the north. We thus modeled the ^{10}Be concentration of the lower four samples with depth, and the best fit of the ^{10}Be data suggests an exposure age of $10^{+0.6}/_{-1.8}$ ka. For the unmodeled sample T2S-00, we then used the online CRONUS calculator v3.0 and obtained an exposure age of 13.5 ± 0.7 ka after the correction of inheritance derived from the depth profile modeling. This age is nearly identical to the abandonment age of the T4 surface ($13.0^{+0.8}/_{-0.2}$ ka) that is located at the top of the scarp, reinforcing our interpretation of colluvial origin for the upper part of the pit section. We thus determined that T2 was abandoned at $10^{+0.6}/_{-1.8}$ ka and covered by colluvium very recently (Table 2).

Figure 9

In summary, the abandonment age of T3 is determined to be $11.1^{+0.4}/_{-0.5}$ ka from a combination of ^{10}Be and OSL dating. The exposure age of terrace T2' yields $10^{+0.6}/_{-1.8}$ ka, based on ^{10}Be dating. These results are consistent with the mean exposure age of 9.1 ± 2.9 ka for terrace T1 at the Hasi Shan piedmont (Matrau et al., 2019). The abandonment age of our terrace T4, $13.0^{+0.8}/_{-0.2}$ ka, is compatible with the age of terrace T2 in Matrau et al. (2019), 15 ± 2 ka.

5 Interpretation and Discussion

5.1 Slip Rate Determination

Dating cumulative offset of risers related to the continuous activity of a strike-slip fault is not straightforward, as risers are transient morphological features (e.g., Weldon & Sieh, 1985; Ryerson et al., 2006; Harkins and Kirby, 2008; Cowgill, 2007; Gold et al., 2009, 2011). In one scenario, a riser is constantly refreshed and laterally eroded by the active river flow until this river has incised enough into the lower terrace, leading to the abandonment of the low terrace. At that point, the surface of the lower terrace, at the base of the riser, is considered as stable and could be used to constrain the accrued offset of the riser (Weldon & Sieh, 1985; Gaudemer et al., 1995; Lasserre et al., 1998, 2002; Van der Woerd et al., 1998; Mériaux et al., 2004). However, this partial rejuvenation of the base of the riser when the river is still actively flowing on the lower terrace might lead to a different amount of offset between the top and the base of the riser. In addition, the top of the riser could start recording slip as soon as the upper terrace is abandoned, while the base

of the riser is dependent on the abandonment of the lower terrace (Cowgill, 2007; Lasserre et al., 1999; Yao et al., 2019). Hence, a detailed analysis of the geomorphic processes is critical to determine an accurate geologic slip rate by utilizing displaced risers. Two key aspects must be considered: (1) well preserved piercing lines recording cumulative displacements and (2) tight constraints on the time period when the record of the offset started.

At the Dougouping site, the well-preserved displaced geomorphic features include the T4/T2' riser, the T3/T3' riser, and the eastern edges of the T4 tread and the T3 tread. We speculate that T4' was formed during the incision of T4; T4' formed only on the northern side of the fault due to the north-side-up vertical component of displacement. Measurement of the T4/T2' riser crest yields an offset of $22.4^{+6.8}_{-4.5}$ m (CC'), whereas the base of the T4/T2' riser is offset $20.6^{+8}_{-4.6}$ m (cc'). The slightly larger offset of the T4/T2' riser crest implies that the riser crest may have continually accrued offset before the abandonment of upper terrace T4. Thus, combining the offset of the T4/T2' riser crest and the abandonment age of T4 could provide a lower bound for the slip rate. On the other hand, the offsets of the crest and base of the T3/T3' riser are consistent with each other (GG', $19.1^{+3.5}_{-3.0}$ m, and FF', $16.8^{+5.7}_{-2.2}$ m). Dividing this mean accrued displacement of the T3/T3' riser crest ($19.1^{+3.5}_{-3.0}$ m) by the exposure age of T3 ($11.1^{+0.4}_{-0.5}$ ka) yields a lower bound slip rate. In addition to these two lower bounds, combining the cumulative displacement of the eastern edge of the T4 tread (11.3^{+5}_{-4} m) with the abandonment age of T4 ($13.0^{+0.8}_{-0.2}$ ka) and the eastern edge of the T3 tread ($12.4^{+1}_{-2.4}$ m) with the abandonment age of T3 ($11.1^{+0.4}_{-0.5}$ ka), both yield minimum left-lateral slip rates, which can also be considered as the lower bound. On the other hand, dividing the offset of the T4/T2' riser base by the abandonment age of T2' yields an upper bound for the slip rate (Table 3).

We associated the age of dated terraces at the Dougouping site with their matching offsets, and we derived different slip rates by using the slip-rate calculator of Styron (2015) with 10000 iterations (Table 3). The uncertainties of offsets and ages in our measurements are considered. First, we include only the riser crests and terrace tread edge together with their matching terrace ages; we obtain a lower bound for the slip rate of 1.4 ± 0.1 mm/yr (Figure 10a). We note that the mean value and the lower bound value are consistent with each other. In the second scenario, we combined the offset of the T4/T2' riser base and the abandonment age of T2', which yields a slip rate of 2.1 ± 0.4 mm/yr (Figure 10b). We consider this rate as an upper bound for the slip rate along the Zihong Shan fault. Their uncertainties were all set with 1σ . Hence, by combining the slip rates of the lower bound (1.4 ± 0.1 mm/yr) and upper bound (2.1 ± 0.4 mm/yr) determined from this study, the average slip rate of the Zihong Shan fault is 1.9 ± 0.6 mm/yr over ~ 13 ka.

Figure 10.

5.2 Strain Partitioning on the Haiyuan Fault

Summing the horizontal slip rate from each individual strand provides an estimation of the rate across the fault system. At the Hasi Shan restraining bend, the Haiyuan fault, splaying into at least four strands, may accommodate oblique strike-slip motion through strike-slip and dip-slip behaviors (Figure 11). Two strands to the south of the Hasi Shan Range show mostly left-lateral strike-slip motion. The southernmost Zihong Shan fault slips at 1.9 ± 0.6 mm/yr since ~ 13 ka; the Hasi Shan south frontal fault is moving at 2.7 ± 0.5 mm/yr since ~ 15 ka (Matrau et al., 2019)

(Figure 11). Brought together, it yields a horizontal slip rate for the two strands south of the Hasi Shan of 4.1 ± 0.6 mm/yr since ~ 15 ka. Two other strands, one, the Liushashui fault, slicing through the interior of the Hasi Shan and another, the Shuanglong fault, bounding the northern front of the Hasi Shan, show linear traces in the topography and offset channels (>30 m offset), as observed on satellite images (Figure 11c). Hence, they might accommodate an additional fraction of the strike-slip motion, although their activity remains to be quantified. In addition, one minor fault, located between the Zihong Shan and Hasi Shan frontal faults horizontally displaces a surface and linked to T1 in Matrau et al. (2019), might also accommodate a minor amount of the total slip of the fault system. Therefore, the summed horizontal slip rate of 4.1 ± 0.6 mm/yr, which includes only the two fault strands to the south of the Hasi Shan, is a minimum slip rate at the Hasi Shan restraining bend (Figure 11a and 11b).

The Haiyuan fault, with a maximum elevation of 2987 m in the rhomb-shaped Hasi Shan Range, indicates local uplift on a geological time scale. Three out of the four fault strands show clear evidence of vertical motion in addition to dominant strike-slip. Among them, along the Zihong Shan fault branch, the north-side-up vertical slip rate is ~ 0.2 - 0.3 mm/yr based on the vertical offset of dated terraces at the Dougouping site. Combining the vertical displacement of the T4/T2' riser crest and the eastern edge of T4 indicates that the vertical displacement of terrace T4 ranges from 3.4 to 4.3 m. By dividing the exposure age of T4 ($13^{+0.8/-0.2}$ ka) thus yields a vertical slip rate of ~ 0.2 - 0.3 mm/yr. Similarly, the vertical offset (1.8~2.4 m) of the dated terrace T3 ($11.1^{+0.4/-0.5}$ ka) suggests a rate of ~ 0.2 mm/yr. In addition, along the Hasi Shan frontal fault, Matrau et al. (2019) derived an uplift rate of 0.4 ± 0.2 mm/yr. The Shuanglong fault, bounding the Hasi Shan Range to the north, also accommodates some vertical uplift of the mountain range, as evidenced by vertical fault scarps up to ~ 6 m cutting through loess-mantled hillslopes at Maweichuan (Figure 11d). These vertical slip rates should then be put together and yield a minimum uplift rate of $0.6^{+0.3/-0.2}$ mm/yr at the Hai Shan section.

Figure 11.

Combining our results with Matrau et al. (2019), this study thus establishes a local framework with a similar slip rate of ~ 5 – 10 mm/yr from $\sim 102.2^\circ\text{E}$ to $\sim 104.5^\circ\text{E}$. However, we cannot exclude a slight decrease in slip rate from 104.5°E eastward (Zhang et al., 1988; Burchfiel et al., 1991; Li et al., 2009). Within the uncertainty in slip rate determination, the minimum horizontal slip rate (4.1 ± 0.6 mm/yr) at the Hasi Shan geometric complexity is slightly smaller than the lower-bound of the recently updated slip rate (5 – 8.9 mm/yr) ~ 80 km to the west along the simple, rectilinear Laohu Shan section (Yao et al., 2019). The slight decrease in the strike-slip component should be compensated by the vertical motion. The vertical deformation rate of at least three strands at the Hasi Shan geometric complexities ranges from 0.4 to 0.9 mm/yr in minimum and accommodates part of the total budget of deformation. Thus, considering the entire geometry and deformation rates (horizontal and vertical), the deformation rate of the Haiyuan fault system at the Hasi Shan section is similar with its neighbor sections. Although the geometric complexity exists in the upper part of the crust, the fault is likely throughgoing at depth. Similar examples include the San Gorgonio Pass section of the San Andreas fault (Bennett et al., 2004; Dair & Cooke, 2009; Burgette et al., 2020) and the Lebanese restraining bend along the Dead Sea fault system (Daeron et al., 2004; Goren et al., 2015). This is important because without quantifying the slip rate of the Zihong Shan fault and its role in strain partitioning in this geometrically complex

region, one might be misled by the apparent slip-rate deficit on the Hasi Shan front fault, which has been traditionally considered as the Haiyuan fault (Deng et al., 1986; IGCEA, 1990; Li et al., 2009; Ren et al., 2015).

5.3 Seismic Potential of the Zihong Shan Fault

Geometric complexities along a fault are defined as critical zones where ruptures would preferably initiate or terminate (e.g., King & Nabelek, 1985; Wesnousky, 1988, 2006; Harris et al., 1991; Shaw, 2006). The Hasi Shan section of the Haiyuan fault, consisting of four strands with strike ($\sim N120^\circ E$) oblique to the overall trend of the fault, behaves as a restraining bend (Figure 11). The 1920 Mw 7.9 Haiyuan earthquake ruptured the southern Hasi Shan frontal fault branch of the bend with a maximum horizontal coseismic slip of ~ 5.6 m (Zhang et al., 1987) or ~ 4 m on average based on LiDAR data and high-resolution images (Zhang et al., 1987; Ren et al., 2015; Ou et al., 2020). A paleoseismic study revealed six paleoearthquakes (in addition to the 1920 Haiyuan earthquake) during the past 10,000 years in this section, suggesting an average recurrence interval of 2000 ± 500 a B.P. (Zhang et al., 2005). In contrast, the activity and earthquake recurrence of the Zihong Shan fault has barely been documented. The slip rate of the Zihong Shan fault determined in this study (1.9 ± 0.6 mm/yr since ~ 13 ka) represents $\sim 70\%$ of the rate on the Hasi Shan frontal fault and could pose a considerable seismic threat unrecognized before in this region.

To estimate the seismic potential of the Zihong Shan fault, we determined the seismic moment for a full-section rupture. We calculated the scalar seismic moment $M_0 = \mu D_{ave} A$, where $\mu = 3 \cdot 10^{10}$ N/m² is the shear modulus for crustal faults (Hanks & Kanamori, 1979), D_{ave} is the average displacement, and A is the fault-plane area (length*width). To define fault width, we assume a nearly vertical fault, which is reasonable for a dominantly strike-slip fault. And thus, the width of the rupture is equivalent to a seismogenic depth of 12-15 km, based on the depth range of large instrumentally recorded earthquakes in the area, the average-depth distribution of crustal seismicity associated with the region, and geodetically derived fault locking depth for strike-slip faults in the region (e.g., Sun et al., 2017; Daout et al., 2016a; Deng et al., 2020). For a full-section rupture (~ 50 km) with a rupture width of 12-15 km, we used the surface-rupture length (SRL) along the fault and the empirical fault-scaling relationships for intraplate strike-slip faults to estimate a scaling-relationship derived $D_{ave} = 1$ to 3 m for a ~ 50 km-long rupture (Wells and Coppersmith, 1994; Leonard, 2010, 2014; Stirling et al., 2002). Depending on the details of the different scaling laws, it yields a total seismic moment release that M_0 ranges consistently between $1.8 \cdot 10^{19}$ - $6.75 \cdot 10^{19}$ Nm, which is equivalent to an Mw 6.8-7.2 earthquake (with $Mw = 2/3 \cdot \log(M_0) - 6$; Kanamori and Anderson, 1975; Hanks and Kanamori, 1979). If we use $D_{ave} = 3.9$ m, the first and largest peak of the offsets COPD (Figure 8b), as the coseismic offset of the most recent earthquake (Klinger et al., 2011; Zielke et al., 2010; Ren et al., 2015; Li et al., 2019), the moment magnitude would be Mw 7.2.

The first COPD peak of offsets was used to identify coseismic offset associated with the most recent earthquake (Klinger et al., 2011; Zielke et al., 2010; Ren et al., 2015; Li et al., 2019), and subsequent peaks may reflect cumulative offsets with an increasing number of earthquakes depending on whether displaced geomorphic markers are sufficient (Kurtz et al., 2018). The first and largest peak (3.9 m) of the COPD of offsets along the Zihong Shan fault is larger than the estimated average displacement (1 to 3 m) based on various surface rupture length-displacement scaling relationships. The increment between the first and second peaks (~ 3 m) is also on the high

end. This may suggest that the Zihong Shan fault is structurally immature if a higher D/L ratio for a given rupture length would be characterizing less matured fault (Liu-Zeng et al., 2005; Manighetti et al., 2007). If so, earthquake rupture on an immature Zihong Shan fault implies a more energetic rupture and higher strong motion and thus potentially more severe earthquake damage than the global average (Manighetti et al., 2007; Radiguet et al., 2009). Alternatively, the first peak might correspond to the cumulative deformation due to more than one event. Geomorphic smoothing of offset features by surface processes would make it more challenging to distinguish single-event or cumulative offsets if coseismic offsets were minor (e.g., a couple of meters) and/or for earthquakes that occurred a long time ago (Gold et al., 2013; Lin et al., 2020).

Many large earthquakes have complex rupture patterns with at least one major branch involved within geometric complexity zones (Harris et al., 2002; Dair & Cook, 2009; Schwart et al., 2012; Klinger et al., 2005, 2018; Choi et al., 2018). The Zihong Shan fault can fail individually or together with other parallel branches. The 1920 Haiyuan earthquake rupture propagated westward through the Hasi Shan bend, following the Hasi Shan front fault strand (Figure 11). It is intriguing why the rupture did not proceed along the Zihong Shan fault, which aligns with the rupture path from the east; instead, the rupture made a 28° degree turn at the junction and branched off on the Hasi Shan Range front fault. Several earthquakes have revealed that the existence of large branches could divert the rupture from the continuous geological trace of the fault. For instance, the 2002 M_w 7.9 Denali earthquake rupture initiated along the central segment of the Denali fault for ~225 km before branching off on the Totschunda fault that deviates from the central fault. The 2001 Kokoxili earthquake rupture also turned 6° clockwise and jumped onto the Kunlun Pass fault instead of continuing onto the more direct Xidatan segment. For the deviation in the 2002 Denali rupture, mechanisms proposed include the effect of past earthquake history along that fault system (Schwart et al., 2012) and dynamic stress conditions as the rupture proceeded at supershear rupture speed (Bhat et al., 2004). A change in the supershear rupture velocity was proposed for the 2001 Kokoxili earthquake rupture (Bouchon & Vallée., 2003). It is not clear whether the rupture dynamic effect played a role in the case of the 1920 earthquake, which occurred 100 years ago and before the era of digital seismographic records. It is possible the Zihong Shan fault is not directly linked to the fault with the eastern incoming rupture. Both in the field and high-resolution satellite images, the 1920 Haiyuan earthquake rupture bounds the Huangliangtan pull-apart basin to the east, then the morphological trace can be followed to the Hasi Shan front fault, but not to the Zihong Shan fault, despite being similar in strike (Figure S14).

Overall, our results reinforce that the potential severity of future earthquakes along the Zihong Shan fault branch should not be ignored and that the seismological history along this fault remains to be deciphered in detail. Unrecognized relatively simple faults within a complex fault geometry system might fail in future destructive earthquakes (Yule & Seih, 2003; Marshall et al., 1991; Jones et al., 1986). Therefore, detailed paleoseismic investigations are needed along the Zihong Shan fault.

6 Conclusions

The use of high-resolution DEMs derived from small uncrewed aerial vehicles combined with field observations along the Zihong Shan fault, a branch of the Haiyuan fault, provides a valuable opportunity to interpret details of tectonic-geomorphic features for Quaternary activity assessments. Using geomorphologic data together with dating constraints, including ^{10}Be depth

profile and OSL dating techniques, we could bracket the sinistral slip rate between 1.3 and 2.5 mm/yr for the last ~13 ka along the Zihong Shan fault. The slip rate is similar to that on the better-known Hasi Shan frontal fault, which ruptured during the 1920 M_w 7.9 Haiyuan earthquake. Combining the two main strands, the total horizontal slip rate of the Haiyuan fault system at this geometric complexity is 4.1 ± 0.6 mm/yr at the minimum, which is slightly less than the slip rate along sections to the east and west. Our results suggest that the vertical deformation of the two main strands and the evident Quaternary activity of the other two northern strands at the Hasi Shan section should not be ignored in the total budget deformation of the Haiyuan fault system. The clustering of the geomorphic left-lateral offsets along the ~50 km-long Zihong Shan fault suggests the first and most pronounced offset on the order of 3.9 m. Assuming one earthquake rupture the entire length of the Zihong Shan fault, it could be with a potential $M_w \sim 7$ earthquake source. The comparable slip rates on the Zihong Shan and Hasi Shan frontal faults suggest that the seismic hazard of the Zihong Shan branch might be greatly underestimated.

Acknowledgments

This project was conducted under the auspices of the National Natural Science Foundation of China (U1839203, 41802228) and the State Key Laboratory of Earthquake Dynamics of China (LED2017A01). YK was partly funded through ANR project DISRUPT (ANR-18-CE31-0012). We thank Huili Yang for her assistance with OSL samples. Arjun Heimsath is also thanked for guidance in the process of CRNs samples. We also thank Zhaode Yuan, Xue Li, Xinyue Xu, and Heng Wang for the fieldwork.

Data Availability Statement

The data used in this research, including the original raster data, are available at <https://zenodo.org/record/6339684#.Yif6EsjASV0>.

References

- Allen, M. B., Walters, R. J., Song, S., Saville, C., Paola, N. D., Ford, J., et al. (2017). Partitioning of oblique convergence coupled to the fault locking behavior of fold-and-thrust belts: Evidence from the Qilian Shan, northeastern Tibetan Plateau. *Tectonics*, 36(9), 1679-1698. <https://doi.org/10.1002/2017TC004476>
- Anderson, R.S., Repka, J. L., & Dick, G.S. (1996). Explicit treatment of inheritance in dating depositional surfaces using in situ ^{10}Be and ^{26}Al . *Geology*, 24(1),47-51. [https://doi.org/10.1130/091-7613\(1996\)024<0047:etoiid>2.3.co;2](https://doi.org/10.1130/091-7613(1996)024<0047:etoiid>2.3.co;2)
- Avouac, J. P., & Tapponnier, P. (1993). Kinematic model of active deformation in central Asia. *Geophysical Research Letters*, 20(10), 895-898. <https://doi.org/10.1029/93GL00128>
- Bennett, R. A., Friedrich, A. M., & Furlong, K. P. (2004). Codependent histories of the San Andreas and San Jacinto fault zones from inversion of fault displacement rates. *Geology*, 32(11), 961–964. <https://doi.org/10.1130/G20806.1>
- Bhat, H. S., Dmowska, R., Rice, J. R., & Kame, N. (2004). Dynamic slip transfer from the Denali to Totschunda faults, Alaska: Testing theory for fault branching. *Bulletin of the Seismological Society of America*, 94(6), S202-S213. <https://doi.org/10.1785/0120040601>

- Blisniuk, K., Rockwell, T., Owen, L. A., Oskin, M., Lippincott, C., Caffee, M. W., et al. (2010). Late quaternary slip rate gradient defined using high-resolution topography and ^{10}Be dating of offset landforms on the southern San Jacinto fault zone, California. *Journal of Geophysical Research Solid Earth*, 115(B8). <https://doi.org/10.1029/2009JB006346>
- Bouchon, M., & Vallée, M. (2003). Observation of long supershear rupture during the magnitude 8.1 Kunlunshan earthquake. *Science*, 301(5634), 824-826. <https://doi.org/10.1126/science.1086832>
- Bowman, D., King, G., and Tapponnier. (2003). Slip Partitioning by Elastoplastic Propagation of Oblique Slip at Depth. *Science*, 300 (5622), 1121-3. <https://doi.org/10.1126/science.1082180>
- Burchfiel, B., Zhang, P. Z., Wang, Y. P., Zhang, W. Q., Song, F. M., Deng, Q. D., et al. (1991). Geology of the Haiyuan fault zone, Ningxia- Hui Autonomous Region, China, and its relation to the evolution of the northeastern margin of the Tibetan Plateau. *Tectonics*, 10(6), 1091-1110. <https://doi.org/10.1029/90TC02685>
- Burgette, R. J., Hanson, A. M., Scharer, K. M., Rittenour, T. M., & McPhillips, D. (2020). Late Quaternary slip rate of the Central Sierra Madre fault, southern California: Implications for slip partitioning and earthquake hazard. *Earth and Planetary Science Letters*, 530, 115907. <https://doi.org/10.1016/j.epsl.2019.115907>
- Cavalié, O., Lasserre, C., Doin, M. P., Peltzer, G., Sun, J., Xu, X., et al. (2008). Measurement of interseismic strain across the Haiyuan fault (Gansu, China), by InSAR. *Earth and Planetary Science Letters*, 275(3-4), 246-257. <https://doi.org/10.1016/j.epsl.2008.07.057>
- Chai C., Jiao D., Liao Y., Zhang S., Du P. & Shen W. (2003). Discovery of surface rupture zone produced by Guanganling earthquake at the juncture of Ningxia, inner Mongolia and Gansu Province (in Chinese). *Seismology and Geology*, 25(1), 167-171.
- Choi, J. H., Klinger, Y., Ferry, M., Ritz, J. F., Kurtz, R., Rizza, M., et al. (2018). Geologic inheritance and earthquake rupture processes: The 1905 $M \geq 8$ Tsetserleg- Bulnay strike-slip earthquake sequence, Mongolia. *Journal of Geophysical Research Solid Earth*, 123(2), 1925-1953. <https://doi.org/10.1002/2017JB013962>
- Cowgill, E. (2007). Impact of riser reconstructions on estimation of secular variation in rates of strike-slip faulting. Revisiting the Cherchen River site along the Altyn Tagh Fault, NW China. *Earth and Planetary Science Letters*, 254(3-4), 239-255. <https://doi.org/10.1016/j.epsl.2006.09.015>
- Cunningham, W. D., & Mann, P. (2007). Tectonics of strike-slip restraining and releasing bends. *Geological Society, London, Special Publications*, 290(1), 1-12. <https://doi.org/10.1144/SP290.1>
- Daëron M., Benedetti, L., Tapponnier, P., Sursock, A., & Finkel, R. C. (2004). Constraints on the post-25-ka slip rate of the Yammouneh fault (Lebanon) using in situ cosmogenic ^{36}Cl dating of offset limestone-clast fans. *Earth and Planetary Science Letters*, 227(1-2), 105-119. <https://doi.org/10.1016/j.epsl.2004.07.014>
- Dair, L., & Cooke, M. L. (2009). San Andreas Fault geometry through the San Gorgonio pass, California. *Geology*, 37(2), 119-122. <https://doi.org/10.1130/G25101A.1>
- Daout, S., Jolivet, R., Lasserre, C., Doin, M. P., Barbot, S., Tapponnier, P., et al. (2016a). Along-strike variations of the partitioning of convergence across the Haiyuan fault system detected by InSAR. *Geophysical Journal International*, 205(1), 536-547. <https://doi.org/10.1093/gji/ggw028>

- Daout, S., Barbot, S., Peltzer, G., Doin, M. P., Liu, Z., & Jolivet, R. (2016b). Constraining the kinematics of metropolitan Los Angeles faults with a slip-partitioning model. *Geophysical research letters*, 43(21), 11192-11201. <https://doi.org/10.1002/2016GL071061>
- Deng, Q., Chen, S., Song, F., Zhu, S., Wang, Y., Zhang, W., & Zhang, P. Z. (1986). Variations in the geometry and amount of slip on the Haiyuan (Nanxihashan) fault zone, China and the surface rupture of the 1920 Haiyuan earthquake, in *Earthquake Source Mechanics* (pp. 169-182). AGU, Washington, D. C.
- Deng, Y., Peng, Z., & Liu - Zeng, J. (2020). Systematic search for repeating earthquakes along the Haiyuan fault system in northeastern Tibet. *Journal of Geophysical Research: Solid Earth*, 125, e2020JB019583. <https://doi.org/10.1029/2020JB019583>
- Fuis, G. S., Ryberg, T., Godfrey, N. J., Okaya, D. A., & Murphy, J. M. (2001). Crustal structure and tectonics from the Los Angeles basin to the Mojave Desert, southern California. *Geology*, 29(1), 15-18. [https://doi.org/10.1130/0091-7613\(2001\)029<0015:CSATFT>2.0.CO;2](https://doi.org/10.1130/0091-7613(2001)029<0015:CSATFT>2.0.CO;2)
- Gaudemer, Y., Tapponnier, P., Meyer, B., Peltzer, G., Guo, S. M., Chen, Z.T., et al. (1995). Partitioning of crustal slip between linked, active faults in the eastern Qilian Shan and evidence for a major seismic gap, the 'Tianzhu gap', on the western Haiyuan Fault, Gansu (China). *Geophysical Journal International*, 120(3), 599-645. <https://doi.org/10.1111/j.1365-246X.1995.tb01842.x>
- Gold, R. D., Cowgill, E., Arrowsmith, J. R., Chen, X., Sharp, W. D., Cooper, K. M., & Wang, X. F. (2011). Faulted terrace risers place new constraints on the late Quaternary slip rate for the central Altyn Tagh fault, northwest Tibet. *Geological Society of America Bulletin*, 123(5-6), 958-978. <https://doi.org/10.1130/B30207.1>
- Gold, R. D., Cowgill, E., Arrowsmith, J. R., Gosse, J., Chen, X. H., & Wang, X. F. (2009). Riser diachroneity, lateral erosion, and uncertainty in rates of strike-slip faulting: A case study from Tuzidun along the Altyn Tagh Fault, NW China. *Journal of Geophysical Research: Solid Earth*, 114, B04401. <https://doi.org/10.1029/2008JB005913>
- Gold, R. D., Stephenson, W. J., Odum, J. K., Briggs, R. W., Crone, A. J., & Angster, S. J. (2013). Concealed Quaternary strike-slip fault resolved with airborne lidar and seismic reflection: The Grizzly Valley fault system, northern Walker Lane, California. *Journal of Geophysical Research: Solid Earth*, 118(7), 3753-3766. <https://doi.org/10.1002/jgrb.50238>
- Goren, L., Castellort, S., & Klingler, Y. (2015). Modes and rates of horizontal deformation from rotated river basins: Application to the Dead Sea fault system in Lebanon. *Geology*, 43(9), 843-846. <https://doi.org/10.1130/G36841.1>
- Gosse, J. C., & Phillips, F. M. (2001). Terrestrial in situ cosmogenic nuclides: theory and application. *Quaternary Science Reviews*, 20(14), 1475-1560. [https://doi.org/10.1016/S0277-3791\(00\)00171-2](https://doi.org/10.1016/S0277-3791(00)00171-2)
- Guo, P., Han, Z. J., Gao, F., Zhu, C. H., & Gai, H. L. (2020). A new tectonic model for the 1927 M8.0 Gulang Earthquake on the NE Tibetan Plateau. *Tectonics*, 39(9). <https://doi.org/10.1029/2020TC006064>
- Haddon, E. K., Amos, C. B., Zielke, O., Jayko, A. S., & Burgmann, R. (2016). Surface slip during large Owens Valley earthquakes. *Geochemistry Geophysics Geosystems*, 17(6), 2239-2269. <https://doi.org/10.1002/2015GC006033>
- Hanks, T. C., and H. Kanamori (1979), A moment magnitude scale, *J. Geophys. Res.*, 84, 2348-2350. <https://doi.org/10.1029/JB084iB05p02348>

- Harkins, N., & Kirby, E. (2008). Fluvial terrace riser degradation and determination of slip rates on strike-slip faults: an example from the Kunlun fault, China. *Geophysical Research Letters*, 35(5), 94-96. <https://doi.org/10.1029/2007GL033073>
- Harris, R. A., Archuleta, R. J., Day, S. M. (1991). Fault steps and the dynamic rupture process: 2-D numerical simulations of a spontaneously propagating shear fracture. *Geophysical Research Letters*, 18(5), 893-896. <https://doi.org/10.1029/91GL01061>
- Harris, R. A., Dolan, J. F., Hartleb, R., & Day, S. M. (2002). The 1999 Izmit, Turkey, earthquake: A 3D dynamic stress transfer model of intraequake triggering. *Bulletin of the Seismological Society of America*, 92(1), 245-255. <https://doi.org/10.1785/0120000825>
- He, W. G., Liu, B. C., Lv, T. Y., Yuan, D. Y., Liu, J. S., & Liu, X. F. (1994). Study on the segmentation of Laohushan fault zone (in Chinese). *Northwestern Seismological Journal*, 16(3), 66-72.
- Hidy, A. J., Gosse, J. C., Pederson, J. L., Mattern, J. P., & Finkel, R. C. (2010). A geologically constrained Monte Carlo approach to modeling exposure ages from profiles of cosmogenic nuclides: an example from Lees Ferry, Arizona. *Geochemistry Geophysics Geosystems*, 11(9). <https://doi.org/10.1029/2010GC003084>
- Institute of Geology, China Earthquake Administration (IGCEA), & Ningxia Bureau of China Earthquake Administration (NBCEA). (1990). *Active Haiyuan Fault Zone Monograph, Special Publication on Active Fault Studies in China (in Chinese)* (pp. 286). Beijing: Seismology House.
- Jiang, W. L., Han, Z. J., Guo, P., Zhang, J. F., Jiao, Q. S., Kang, S., & Tian, Y. F. (2017). Slip rate and recurrence intervals of the east Lenglongling fault constrained by morphotectonics: Tectonic implications for the northeastern Tibetan Plateau. *Lithosphere*, 9(3), 417-430. <https://doi.org/10.1130/L597.1>
- Jolivet, R., Lasserre, C., Doin, M. P., Peltzer, G., Avouac, J. P., Sun, J., & Dailu, R. (2013). Spatio-temporal evolution of aseismic slip along the Haiyuan fault, China. Implications for fault frictional properties. *Earth and Planetary Science Letters*, 377-378, 23-33. <https://doi.org/10.1016/j.epsl.2013.07.020>
- Jones, C. H., & Wesnousky, S. G. (1992). Variations in strength and slip rate along the San Andreas fault system. *Science*, 256(5053), 83-86. <https://doi.org/>
- Jones, L. M., Hutton, L. K., Given, D. D., & Allen, C. R. (1986). The North Palm Springs, California, earthquake sequence of July 1986. *Bulletin of the Seismological Society of America*, 76 (6): 1830-1837. <https://doi.org/10.1785/BSSA0760061830>
- Kanamori, H., and D. L. Anderson (1975). Theoretical basis of some empirical relations in seismology, *Bull. Seismol. Soc. Am.* 65, no. 5, 1073-1095.
- Kendrick, K. J., Morton, D. M., Wells, S. G., & Simpson, R. W. (2002). Spatial and temporal deformation along the northern San Jacinto fault, southern California: Implications for slip rates. *Bulletin of the Seismological Society of America*, 92, 2782-2802. <https://doi.org/10.1785/0120000615>
- King, G., & Nabelek, J. (1985). Role of fault bends in the initiation and termination of earthquake rupture. *Science*, 228(4702), 984-987. <https://doi.org/10.1126/science.228.4702.984>
- Klinger, Y. (2010). Relation between continental strike-slip earthquake segmentation and thickness of the crust. *Journal of Geophysical Research Solid Earth*, 115(B7). <https://doi.org/10.1029/2009JB006550>
- Klinger, Y., Etchebes, M., Tapponnier, P., & Narteau, C. (2011). Characteristic slip for five great earthquakes along the Fuyun fault in China. *Nature Geoscience*, 4(6), 389-392. <https://doi.org/10.1038/NNGEO1158>

- Klinger, Y., Okubo, K., Vallage, A., Champenois, J., Delorme, A., Rougier, E., et al. (2018). Earthquake damage patterns resolve complex rupture processes. *Geophysical Research Letters*, 45(19), 10279-10287. <https://doi.org/10.1029/2018GL078842>
- Klinger, Y., Xu, X. W., Tapponnier, P., Van der Woerd, J., Lasserre, C., & King, G. (2005). High-resolution satellite imagery mapping of the surface rupture and slip distribution of the Mw~7.8, 14 November 2001 Kokoxili earthquake, Kunlun fault, northern Tibet, China. *Bulletin of the Seismological Society of America*, 95(5), 1970-1987. <https://doi.org/10.1785/0120040233>
- Kurtz, R., Klinger, Y., Ferry, M., & Ritz, J.-F. (2018). Horizontal surface-slip distribution through several seismic cycles: The Eastern Bogd fault, Gobi-Altai, Mongolia. *Tectonophysics*, 734-735, 167-182. <https://doi.org/10.1016/j.tecto.2018.03.011>
- Lasserre, C., Gaudemer, Y., Tapponnier, P., Mériaux, A.S., Van der Woerd, J., Yuan, D. Y., et al. (2002). Fast late Pleistocene slip rate on the Leng Long Ling segment of the Haiyuan fault, Qinghai, China. *Journal of Geophysical Research Solid Earth*, 107(B11), 2276. <https://doi.org/10.1029/2000JB000060>
- Lasserre, C., Morel, P. H., Gaudemer, Y., Tapponnier, P., Ryerson, F., King, G., et al. (1999). Postglacial left slip rate and past occurrence of $M \geq 8$ earthquakes on the western Haiyuan fault, Gansu, China. *Journal of Geophysical Research Solid Earth*, 104(B8), 17633-17651. <https://doi.org/10.1029/1998JB900082>
- Leonard, M. (2010). Earthquake fault scaling: Relating rupture length, width, average displacement, and moment release, *Bull. Seismol. Soc. Am.* 100, no. 5, 1971-1988.
- Leonard, M. (2014). Self - consistent earthquake fault - scaling relations: Update and extension to stable continental strike - slip faults. *Bulletin of the Seismological Society of America*, 104(6), 2953-2965. <https://doi.org/10.1785/0120140087>
- Li, C. Y., Zhang, P. Z., Yin, J. H., & Min, W. (2009). Late Quaternary left- lateral slip rate of the Haiyuan fault, northeastern margin of the Tibetan Plateau. *Tectonics*, 28(5). <https://doi.org/10.1029/2008TC002302>
- Li C X, Xu X W, Wen X Z, et al. Rupture segmentation and slip partitioning of the mid-eastern part of the Kunlun Fault, north Tibetan Plateau. *Sci China Earth Sci*, 2011, 54: 1730-1745. <https://doi.org/10.1007/s11430-011-4239-5>
- Li, X. N., Li, C. Y., Pierce, I. K. D., Zhang, P. Z., Zheng, W. J., Dong, J. Y., et al. (2019). New slip rates for the Tianjingshan fault using optically simulated luminescence, GPS, and paleoseismic data, NE Tibet, China. *Tectonophysics*, 755, 64-74. <https://doi.org/10.1016/j.tecto.2019.02.007>
- Lian, O. B., & Roberts, R. G. (2006). Dating the Quaternary: progress in luminescence dating of sediments. *Quaternary Science Reviews*, 25(19-20), 2449-2468. <https://doi.org/10.1016/j.quascirev.2005.11.013>
- Lin, Z., Liu-Zeng, J., Weldon II, R. J., Tian, J., Ding, C., & Du, Y. (2020). Modeling repeated coseismic slip to identify and characterize individual earthquakes from geomorphic offsets on strike-slip faults. *Earth and Planetary Science Letters*, 545, 116313. <https://doi.org/10.1016/j.epsl.2020.116313>
- Liu-Zeng, J., Heaton, T., & DiCaprio, C. (2005). The effect of slip variability on earthquake slip-length scaling. *Geophysical Journal International*, 162(3), 841-849. <https://doi.org/10.1111/j.1365-246X.2005.02679.x>
- Liu, B. C., Yuan, D. Y., He, W. G., & Liu, X. F. (1992). The strong earthquake hazard analysis of the western Haiyuan fault zone (in Chinese). *Journal of Seismic Engineering*, 51, 49-56.

- Manighetti, I., Campillo, M., Bouley, S., & Cotton, F. (2007). Earthquake scaling, fault segmentation, and structural maturity. *Earth and Planetary Science Letters*, 253(3-4), 429-438. <https://doi.org/10.1016/j.epsl.2006.11.004>
- Manighetti, I., Perrin, C., Dominguez, S., Garambois, S., Gaudemer, Y., Malavieille, J., et al. (2015). Recovering paleoearthquake slip record in a highly dynamic alluvial and tectonic region (Hope Fault, New Zealand) from airborne lidar. *Journal of Geophysical Research Solid Earth*, 120(6), 4484–4509. <https://doi.org/10.1002/2014JB011787>
- Marshall, G. A., Stein, R. S., & Thatcher, W. (1991). Faulting geometry and slip from co-seismic elevation changes: The 18 October 1989, Loma Prieta, California, earthquake. *Bulletin of the Seismological Society of America*, 81(5), 1660-1693. <https://doi.org/10.1785/BSSA0810051660>
- Matrau, R., Klinger, Y., Van der Woerd, J., Liu- Zeng, J., Li, Z., Xu, X., & Zheng, R. (2019). Late Pleistocene- Holocene Slip Rate Along the Hasi Shan Restraining Bend of the Haiyuan Fault: Implication for Faulting Dynamics of a Complex Fault System. *Tectonics*, 38(12), 4127-4154. <https://doi.org/10.1029/2019TC005488>
- Mériaux, A. S., Ryerson, F., Tapponnier, P., Van der Woerd, J., Finkel, R., Xu, X., et al. (2004). Rapid slip along the central Altyn Tagh Fault: Morphochronologic evidence from Cherchen He and Sulamu Tagh. *Journal of Geophysical Research Solid Earth*, 109(B6). <https://doi.org/10.1029/2003JB002558>
- Min, W., Zhang, P.Z., & Deng, Q. D. (2001). The study of Holocene Paleoequakes on Zhongwei-Tongxin Fault zone (in Chinese). *Seismology and Geology*, 23 (3), 357–366.
- Norris, R. J., & Cooper, A. F. (2000). Late quaternary slip rates and slip partitioning on the Alpine fault, New Zealand. *Journal of Structural Geology*, 23(2), 507-520. [https://doi.org/10.1016/S0191-8141\(00\)00122-X](https://doi.org/10.1016/S0191-8141(00)00122-X)
- Onderdonk, N. W., McGill, S. F., & Rockwell, T. K. (2015). Short-term variations in slip rate and size of prehistoric earthquakes during the past 2000 years on the northern San Jacinto fault zone, a major plate-boundary structure in southern California. *Lithosphere*, 7(3), 211-234. <https://doi.org/10.1130/L393.1>
- Ou, Q., Kulikova, G., Yu, J., Elliott, A., Parsons, B., & Walker, R. (2020). Magnitude of the 19-20 Haiyuan earthquake reestimated using seismological and geomorphological methods. *Journal of Geophysical Research Solid Earth*, 125(8), e2019JB019244. <https://doi.org/10.1029/2019JB019244>
- Radiguet, M., Cotton, F., Manighetti, I., Campillo, M., & Douglas, J. (2009). Dependency of near-field ground motions on the structural maturity of the ruptured faults. *Bulletin of the Seismological Society of America*, 99(4), 2572-2581. <https://doi.org/10.1785/0120080340>
- Ren, Z. K., Zhang, Z. Q., Chen, T., Yan, S. L., Yin, J. H., Zhang, P. Z., et al. (2015). Clustering of offsets on the Haiyuan fault and their relationship to paleoearthquakes. *Geological Society of America Bulletin*, 128(1-2), 3-18. <https://doi.org/10.1130/B31155.1>
- Rhodes, E. J. (2011). Optically stimulated luminescence dating of sediments over the past 200,000 years. *Annual Review of Earth and Planetary Sciences*, 39(1), 461-488. <https://doi.org/10.1146/annurev-earth-040610-133425>
- Ryerson, F. J., Tapponnier, P., Finkel, R. C., Mériaux, A. S., Van der Woerd, J., Lasserre, C., & et al. (2006). Applications of morphochronology to the active tectonics of Tibet. *Geological Society of America Special Paper*, 415(05), 61-86. [https://doi.org/10.1130/2006.2415\(05\)](https://doi.org/10.1130/2006.2415(05))
- Shao, Y. X., Liu-Zeng, J., Van der Woerd, J., Klinger, Y., Oskin, M. E., Zhang, J. Y., et al. (2021). Late Pleistocene slip rate of the central Haiyuan fault constrained from optically stimulated

- luminescence, ^{14}C , and cosmogenic isotope dating and high-resolution topography. *Geological Society of America Bulletin*, 133(7-8), 1347-1369. <https://doi.org/10.1130/B35571.1>
- Shaw, B. W. (2006). Initiation propagation and termination of elastodynamic ruptures associated with segmentation of faults and shaking hazard. *Journal of Geophysical Research Solid Earth*, 111(B8). <https://doi.org/10.1029/2005JB004093>
- Schwartz, D. P., Haeussler, P. J., Seitz, G. G., & Dawson, T. (2012). Why the 2002 Denali fault rupture propagated onto the Totschunda fault: implications for fault branching and seismic hazards. *Journal of Geophysical Research Solid Earth*, 117(B11). <https://doi.org/10.1029/2011JB008918>
- Stewart, N., Gaudemer, Y., Manighetti, I., Serreau, L., Vincendeau, A., Dominguez, S., et al. (2018). “3D_Fault_Offsets,” a Matlab code to automatically measure lateral and vertical fault offsets in topographic data: Application to San Andreas, Owens Valley, and Hope faults. *Journal of Geophysical Research Solid Earth*, 123(1), 815–835. <https://doi.org/10.1002/2017JB014863>
- Stirling, M., Rhoades, D., & Berryman, K. (2002). Comparison of earthquake scaling relations derived from data of the instrumental and preinstrumental era. *Bulletin of the Seismological Society of America*, 92(2), 812-830. <https://doi.org/10.1785/0120000221>
- Styron, R. (2015). Slip - rate calculator, edited. https://github.com/cossatot/slip_rate_calculator.
- Sun He, Xu Jing, Liu Haoyuan. (2017). Depth Present-Day Movement in the Mid-Eastern Segment of the Haiyuan Fault Zone Based on InSAR (In Chinese). *Journal of Geodesy and Geodynamics*, 37(11): 1141-1145. 10.14075/j.jgg.2017.11.009
- Sylvester, A. G. (1988). Strike-slip faults. *Geological Society of America Bulletin*, 100(11), 1666-1703. [https://doi.org/10.1130/0016-7606\(1988\)100<1666:SSF>2.3.CO;2](https://doi.org/10.1130/0016-7606(1988)100<1666:SSF>2.3.CO;2)
- Tapponnier, P., & Molnar, P. (1976). Active faulting and tectonics in China. *Journal of Geophysical Research*, 82, 2905–2930. <https://doi.org/10.1029/JB082i020p02905>
- Tapponnier, P., Zhiqin, X., Roger, F., Meyer, B., Arnaud, N., Wittlinger, G., & Yang, J. S. (2001), Oblique stepwise rise and growth of the Tibet Plateau. *Science*, 294(5547), 1671-1677. <https://doi.org/10.1126/science.105978>
- Thompson, J. A., Chen, J., Yang, H. L., Li, T., Bookhagen, B., & Burbank, D. (2018). Coarse-versus fine-grain quartz OSL and cosmogenic ^{10}Be dating of deformed fluvial terraces on the north-east Pamir margin, northwest China. *Quaternary Geochronology*, 46, 1-15. <https://doi.org/10.1016/j.quageo.2018.01.002>
- Thompson, S. C., Weldon, R. J., Rubin, C. M., Abdrakhmatov, K., Molnar, P., & Berger, G. W. (2002). Late quaternary slip rates across the central Tien Shan, Kyrgyzstan, central Asia. *Journal of Geophysical Research Solid Earth*, 107(B9). <https://doi.org/10.1029/2001JB000596>
- Tian Q.J., Shen X.H., Ding G.Y., Chen Z.W., Wei K.B., Xing C.Q., & Chai Z. Z. (2000). Discovery and Preliminary study of the Laolongwan Tertiary Pull-apart Basin in the Haiyuan Fault Zone (in Chinese). *Seismology and Geology*, 22(3), 329-336.
- Van der Woerd, J., Ryerson, F., Tapponnier, P., Gaudemer, Y., Finkel, R., Mériaux, A. S., et al. (1998). Holocene left-slip rate determined by cosmogenic surface dating on the Xidatan segment of the Kunlun fault (Qinghai, China). *Geology*, 26(8), 695-698. [https://doi.org/10.1130/0091-7613\(1998\)026<0695:HLSRDB>2.3.CO;2](https://doi.org/10.1130/0091-7613(1998)026<0695:HLSRDB>2.3.CO;2)
- Wells, D. L., and K. J. Coppersmith. (1994). New empirical relationships among magnitude, rupture length, rupture width, rupture area, and surface displacement, *Bull. Seismol. Soc. Am.*, 84(4), 974–1002. <https://doi.org/10.1785/BSSA0840040974>
- Weldon, R. J., & Sieh, K. E. (1985). Holocene rate of slip and tentative recurrence interval for large earthquakes on the San Andreas fault, Cajon Pass, southern California. *Geological Society*

of America Bulletin, 96(6), 793-812. [https://doi.org/10.1130/0016-7606\(1985\)96<793:HROSA T>2.0.CO;2](https://doi.org/10.1130/0016-7606(1985)96<793:HROSA T>2.0.CO;2)

- Wesnousky, S. G. (1988). Seismological and structural evolution of strike-slip faults. *Nature*, 335(6188), 340–343. <https://doi.org/10.1038/335340a0>
- Wesnousky, S. G. (2006). Predicting the endpoints of earthquake ruptures. *Nature*, 444(7117), 358–360. <https://doi.org/10.1038/nature05275>
- Yang, H. B., Yang, X. S., Huang, X. N., Li, A., Huang, W. L., & Zhang, L. (2018). New constraints on slip rates of the Fodongmiao- Hongyazi fault in the Northern Qilian Shan, NE Tibet, from the ¹⁰Be exposure dating of offset terraces. *Journal of Asian Earth Sciences*, 151, 131–147. <https://doi.org/10.1016/j.jseaes.2017.10.034>
- Yao, W. Q., Liu- Zeng, J., Oskin, M. E., Wang, W., Li, Z., Prush, V., et al. (2019). Reevaluation of the Late Pleistocene slip rate of the Haiyuan fault near Songshan, Gansu province, China. *Journal of Geophysical Research Solid Earth*, 124(5), 5217-5240. <https://doi.org/10.1029/2018JB016907>
- Yuan, D. Y., Liu, B. C., Lv, T. Y., He, W. G., Liu, X. F., & Gan, W. J. (1998). Study on the segmentation in east segment of the northern Qilianshan fault zone (in Chinese). *Northwestern Seismological Journal*, 20, 27–34.
- Yule, D., & Sieh, K. (2003). Complexities of the San Andreas fault near San Gorgonio Pass: Implications for large earthquakes. *Journal of Geophysical Research Solid Earth*, 108(B11), 2548. <https://doi.org/10.1029/2001JB000451>
- Zhang, P. Z., Min, W., Deng, Q. D., & Mao, F. Y. (2005). Paleoearthquake rupture behavior and recurrence of great earthquakes along the Haiyuan fault, northwestern China. *Science in China Series D*, 48(3), 364. <https://doi.org/10.1360/02yd0464>
- Zhang, P. Z., Molnar, P., Burchfiel, B., Royden, L., Wang, Y. P., Deng, Q. D., et al. (1988). Bounds on the Holocene slip rate of the Haiyuan fault, north-central China. *Quaternary Research*, 30(2), 151-164. [https://doi.org/10.1016/0033-5894\(88\)90020-8](https://doi.org/10.1016/0033-5894(88)90020-8)
- Zheng, G., Wang, H., Wright, T. J., Lou, Y. D., Zhang, R., Zhang, W. X., et al. (2017), Crustal deformation in the India- Eurasia collision zone from 25 years of GPS measurements. *Journal of Geophysical Research Solid Earth*, 122(11), 9290–9312. <https://doi.org/10.1002/2017JB014465>
- Zielke, O., & Arrowsmith, J. R. (2012). LaDiCaoz and lidar imager—MATLAB GUIs for lidar data handling and lateral displacement measurement. *Geosphere*, 8(1), 206–221. <https://doi.org/10.1130/GES00686.1>
- Zielke, O., Arrowsmith, J. R., Ludwig, L. G., & Akciz, S. O. (2010). Slip in the 1857 and earlier large earthquakes along the Carrizo section, San Andreas Fault. *Science*, 327(5969), 1119-1122. <https://doi.org/10.1002/2017JB014465>
- Zinke, R., Dolan, J. F., Rhodes, E. J., Van Dissen, R., McGuire, C. P., Hatem, A. E., et al. (2019). Multimillennial incremental slip rate variability of the Clarence fault at the Tophouse Road site, Marlborough fault system, New Zealand. *Geophysical Research Letters*, 46(2), 717-725. <https://doi.org/10.1029/2018GL080688>

Figure 1. Active faults in the Northeastern Tibetan Plateau. (a) Map showing the main active faults of the northeastern Tibetan Plateau based on Shuttle Radar Topography Mission data with a 30-m resolution. Green stars are historical earthquakes on the Haiyuan Fault. A black rectangle outlines Figure 2. The Haiyuan fault is subdivided into seven sections, from west to east: HLH = Hala Hu, LLL = Lenglong Ling, JQH = Jinqiang He, MMS = Maomao Shan, LHS = Laohu Shan, HYF = Haiyuan Fault (in the narrow sense), and LPS = Liupan Shan. Abbreviations: ATF = Altyn Tagh Fault, YMF = Yumushan Fault, CMF = Changma Fault, LSSF = Longshoushan Fault, RYSF = Riyueshan Fault, ELSF = Elasha Fault, GLF = Gulang Fault, and ZWF = Zhongwei Fault. (b) Map of active faults and location of the Haiyuan fault in Tibet.

Figure 2. Close-up of the tectonic setting of the study area. (a) Tectonic setting of the study area and location of slip rates from previous studies along the Laohushan section and the Haiyuan fault (in the narrow sense). Colored rectangles are light blue = lower bound rates, purple = upper bound rate, white = unclassified rates, and dark green = lower and upper bound rates. A black rectangle outlines Figure 2b. (b) Geological and structural map of the Mijia Shan-Hasi Shan area, modified from the 1:200,000 scale geological map of Jingtai over a 30-m resolution hillshade. The Surface rupture of the 1920 *M*_w 7.9 Haiyuan earthquake is highlighted with a dark red line. Abbreviations: ZHSF: Zihong Shan Fault; LSSF: Liushashui Fault; SLF: Shuanglong Fault; SM: Shimen; DGP: Dougouping; LLWB: Laolongwan Basin; and HLTB: Huangliangtan Basin.

Figure 3. Shimen site: (a) Orthomosaic photo of the Shimen site. Dark red inverted triangles indicate the trace of the Zihong Shan fault goes. (b) Detailed geomorphic interpretation of the Shimen site. Blue and green dashed lines indicate near- and far-field piercing lines for offset measurements, respectively. White squares mark projected points on the fault. Black dashed lines show topographic profiles in Figure 3c and 3d. (c) and (d) are topographic profiles parallel and perpendicular to the fault, respectively. (e) and (f) are field photos showing a 2.6 m vertical offset of the fault. (g) and (h) are reconstructions showing displacements of the eastern edge of f3 and surface drainages incised into f3.

Figure 4. The Zihong Shan fault trace along the Dougou Ping site: (a) Orthomosaic photos with 0.4 m resolution. (b) 0.8 m resolution DEM-derived slopeshade map overlapped by 1 m contour lines of the Dougouping site. Red inverted triangles indicate the Zihong Shan Fault trace. Dark red and blue rectangles outline Figures 5 and 6, respectively.

Figure 5. The eastern section of the Dougou Ping site: (a) Slopeshade map of the eastern part at the Dougouping site overlapped by 1 m interval contour lines. Black dashed lines is topographic profile shown in Figure 5b. (b) is topographic profile parallel to the Zihong Shan Fault, respectively. (c) and (d) are field photos showing NE-looking views of the emplaced terraces and vertical motion of the fault, respectively. Viewpoints are indicated in Figure 5a. (e) Geomorphic interpretation of the eastern part at the Dougouping site. The positions of the depth profile for terrace surface dating are also shown. The purple dashed rectangle shows Figure 5g. (f) Piercing

lines and projected points of the displacement measurement are shown as dashed lines and color circles.

Figure 6. The western section of the Dougou Ping site: (a) Slopeshade map of the western part of the Dougouping site indicates linear fault traces and inset terraces. The black dashed line is the topographic profile shown in Figure 6b. (b) Fault parallel topographic profile indicating inset terraces. (c) Field photo with SE-looking view, incorporating terraces of the eastern part. (d) Detailed geomorphic mapping. (e) Piercing lines and points of displacement measurements are shown as dashed lines and color circles.

Figure 7. The Yaoshui Gou site: (a) Hillshade map of the Yaoshuigou site with a sketch of the Zihong Shan Fault and oblique secondary faults. Red and blue rectangles outline Figure 7e and 7f, respectively. View locations of field photos are also shown. (b) Perspective view with NE-looking view. (c) and (d) Field photos showing offset channels. (e) SE view of the left-lateral displacement section. (g) and (f) Reconstruction showing offset measurements of channels and ridges.

Figure 8. (a) Geometric distribution of the Zihong Shan fault based on the detailed hillshade relief map derived from the high-resolution DEM. The green dots are offset measurements sites along the Zihong Shan fault. (b) Horizontal offset measurements against distance along the fault. (c) The cumulative offset probability density of the fault. The highest peak forms a wide and well-separated peak at 3.9 m.

Figure 9. Photos with detailed stratigraphic observations and exposure age constraints derived from sand samples with cosmogenic radionuclide depth profiles at the Dougouping site for T4 (a), T3 (b), and T2' (c).

Figure 10. Slip rates at the Dougouping site are calculated using the Bayesian approach from Styron (2015). (a) Slip rate determined as the lower bound by combining the riser crest and tread edge with corresponding age data. (b) Slip rate determined as the upper bound by combining T4'/T2' riser base offset with corresponding age data.

Figure 11. (a) 3D cartoon illuminating the complex fault system at the Hasi Shan with a topographic map derived from 30-m resolution Shuttle Radar Topography Mission data on top. Additionally, the slip rates along the Laohu Shan section and the Hasi Shan complex geometric “knot” are shown. The light green arrow indicates the block motion direction. The green star indicates the site preserved left-lateral offset channels along the Shuanglong fault. (b) Fault trace map of the Hasi Shan restraining bend. (c) High-resolution Google Earth image of the offset channels along the Shuanglong fault. The red line is the fault trace, the green lines mark the piercing lines of the offset measurement, and the white squares are the piercing points. (d) Field photo showing the vertical displacement of the Shuanglong fault (SLF).

Table 1.*Quartz OSL dating results from the Dougouping site with equivalent doses (DE), dosimetry data, and ages*

Terrace	Sample ID	Lab ID	Sample Depth (cm)	Sample Location	Measuring technique	U-238 (Bg/kg)	Ra-226 (Bg/kg)	Th-232 (Bg/kg)	K-40 (Bg/kg)	Water content measured (%)	Environmental dose (Gy/ka)	Equivalent dose (Gy)	Age (ka)
T4N	170717-02-65	LED17-231	65	interbedded sand lens	SA-SGC	20.6±4.7	21.2±0.4	39.4±0.6	497.9±10.0	4.0773	2.7±0.1	36.6±1.8	13.5±1.1
T3N	170719-01-130	LED17-232	130	interbedded sand lens	SA-SGC	26.5±4.8	17.9±0.4	37.9±0.6	476.7±9.8	1.6949	2.7±0.1	49.9±5.7	18.9±2.3

Table 2.
Measured ^{10}Be concentrations at the Dougouping Site, Zihong Shan Fault

Trench	Sample ID	Latitude(°N)	Longitude(°E)	Elevation (m)	Depth ^a (cm)	Thickness (cm)	Shielding	$^{10}\text{Be}/^9\text{Be}$	^{10}Be concentration (atoms/g)	
									Value	Error
T4N	170717-02-20	36.932476	104.369247	1480	20	5	1	1.2544E-13	145283.17	4943.609
	170717-02-40				40			1.0346E-13	121443.03	3982.235
	170717-02-100				100			7.9450E-14	96815.44	3180.896
	170717-02-180				180			7.0991E-14	53301.42	1353.494
T3N	170719-00	36.93217	104.370017	1477	0	5	5	2.2813E-13	161848.05	7444.629
	170719-30				30			1.7594E-13	137174.46	4044.681
	170719-60				60			1.9167E-13	106662.94	3145.028
	170719-120				120			1.3670E-13	80170.54	2647.548
	170719-200				200			4.9496E-14	66559.60	4239.117
T2'S	170717-01-00	36.932094	104.368317	1471	0	5	1	2.0898E-13	171599.68	8517.056
	170717-01-30				30			2.2901E-13	159665.83	8367.684
	170717-01-60				60			1.5686E-13	135471.01	5745.945
	170717-01-120				120			7.8098E-14	88235.67	2061.274
	170717-01-200				200			4.3270E-14	53738.59	961.842

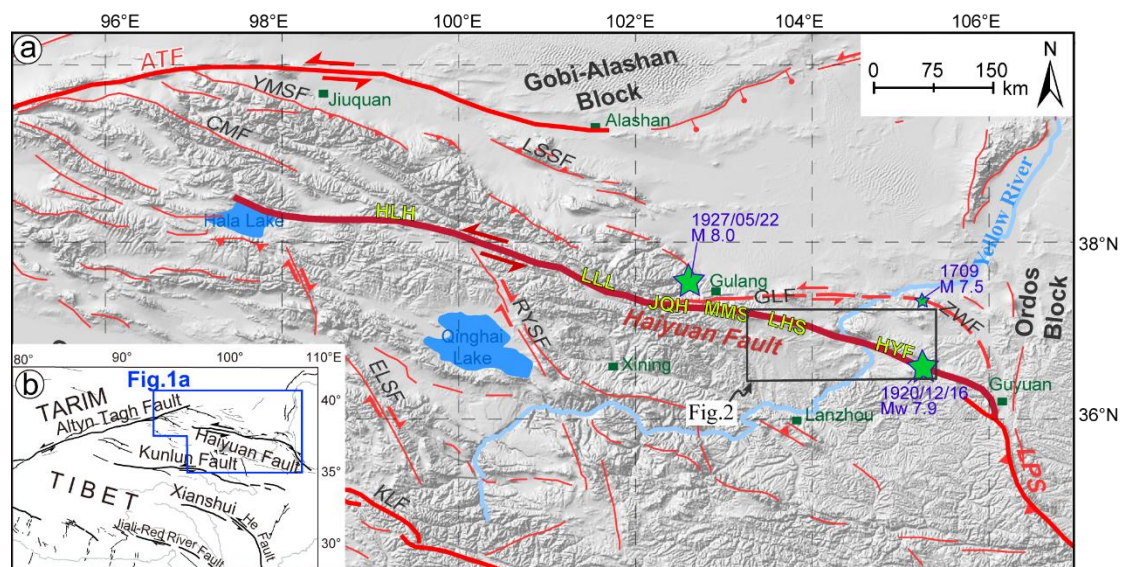
Note.

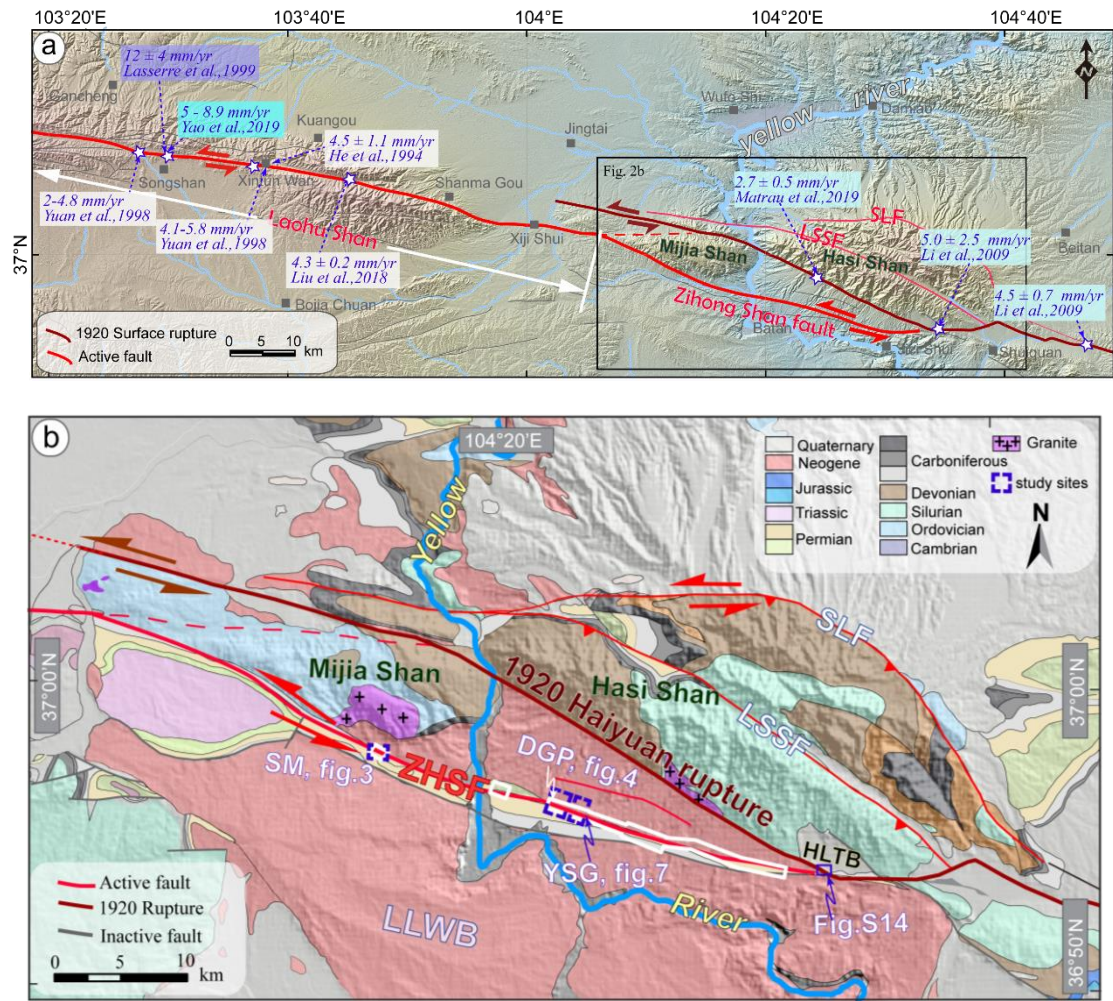
^a Depth beneath the surface

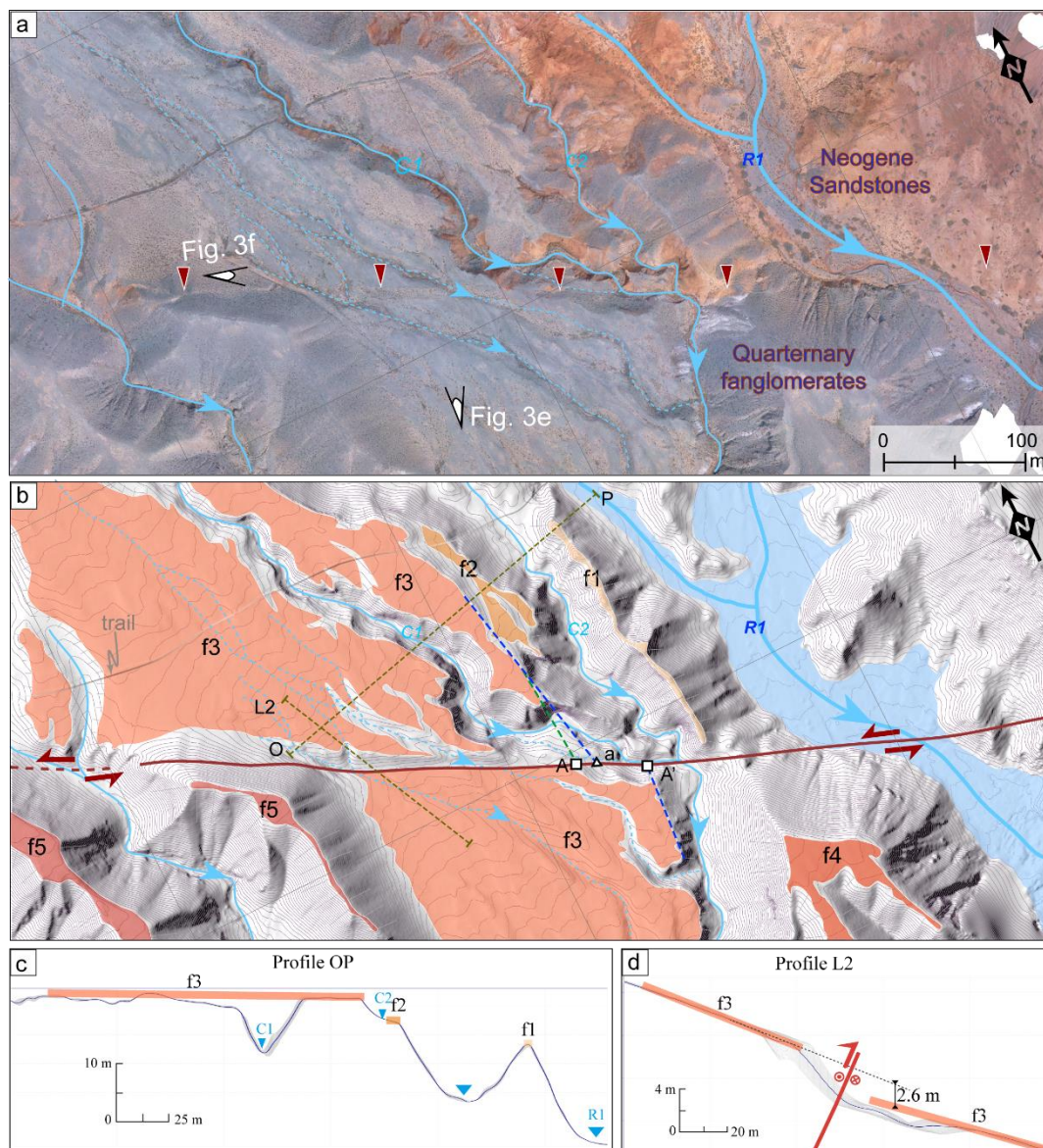
Table 3*Summary of Terrace Riser Offsets and Ages at the Dougou Ping site, Zihong Shan fault*

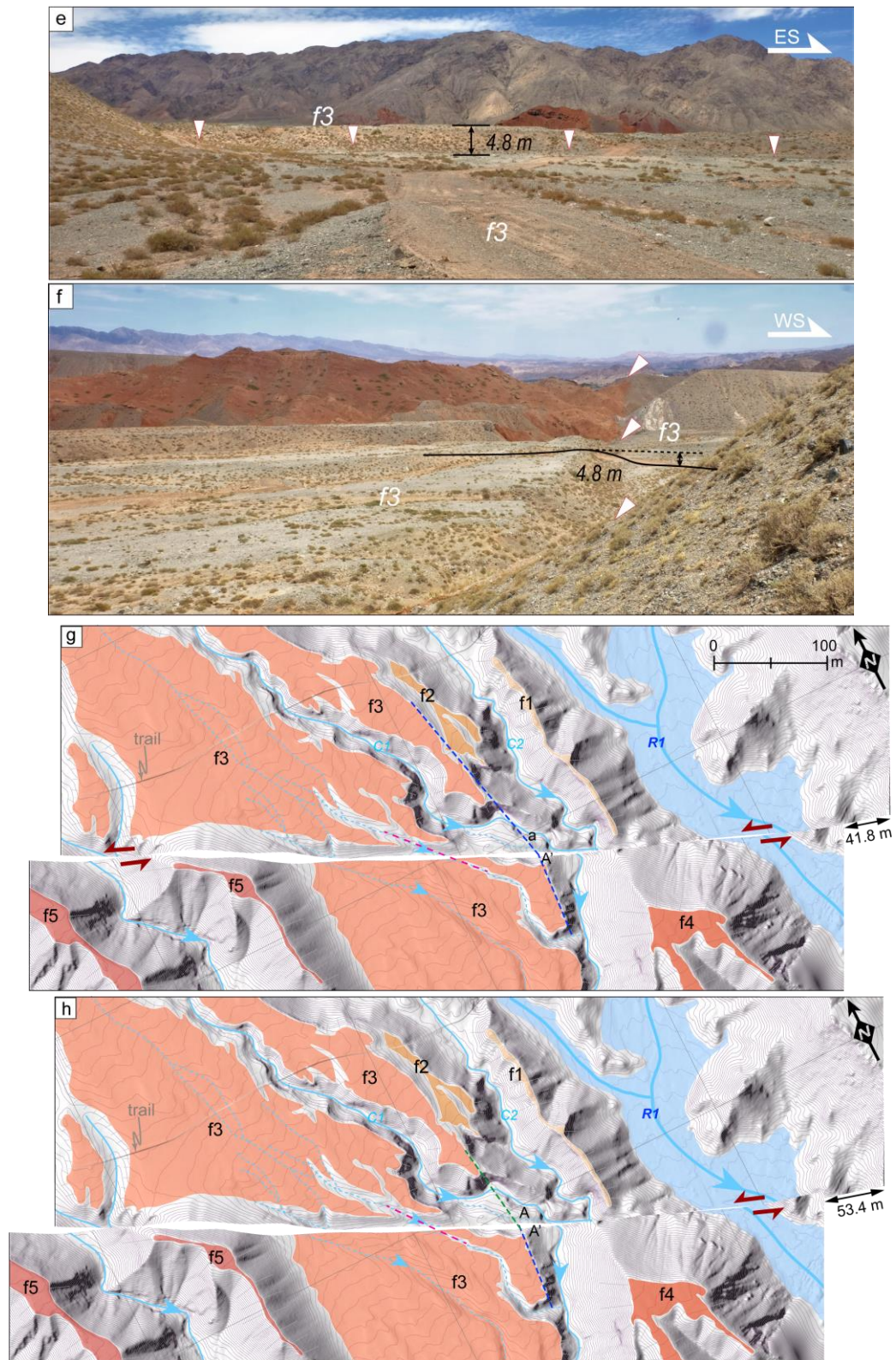
Geomophic markers	Offset (m)	error + (m)	error - (m)	Surface	Age (ka)	error + (ka)	error - (ka)	Slip Rates (mm/yr)	Note
T4/T2' base (cc')	20.6	8.0	4.6	T2'	10.0	0.6	1.8	2.1 ± 0.4	Upper bound
T4/T2' crest (CC')	22.4	6.8	4.5	T4	13.0	0.8	0.2		
T4 tread (DD')	11.3	5.0	4.0	T4	13.0	0.8	0.2	1.4 ± 0.1	Lower bound
T3/T3' crest (GG')	19.1	3.5	3.0	T3	11.1	0.4	0.5		
T3 tread (HH')	12.4	1.0	2.4	T3	11.1	0.4	0.5		

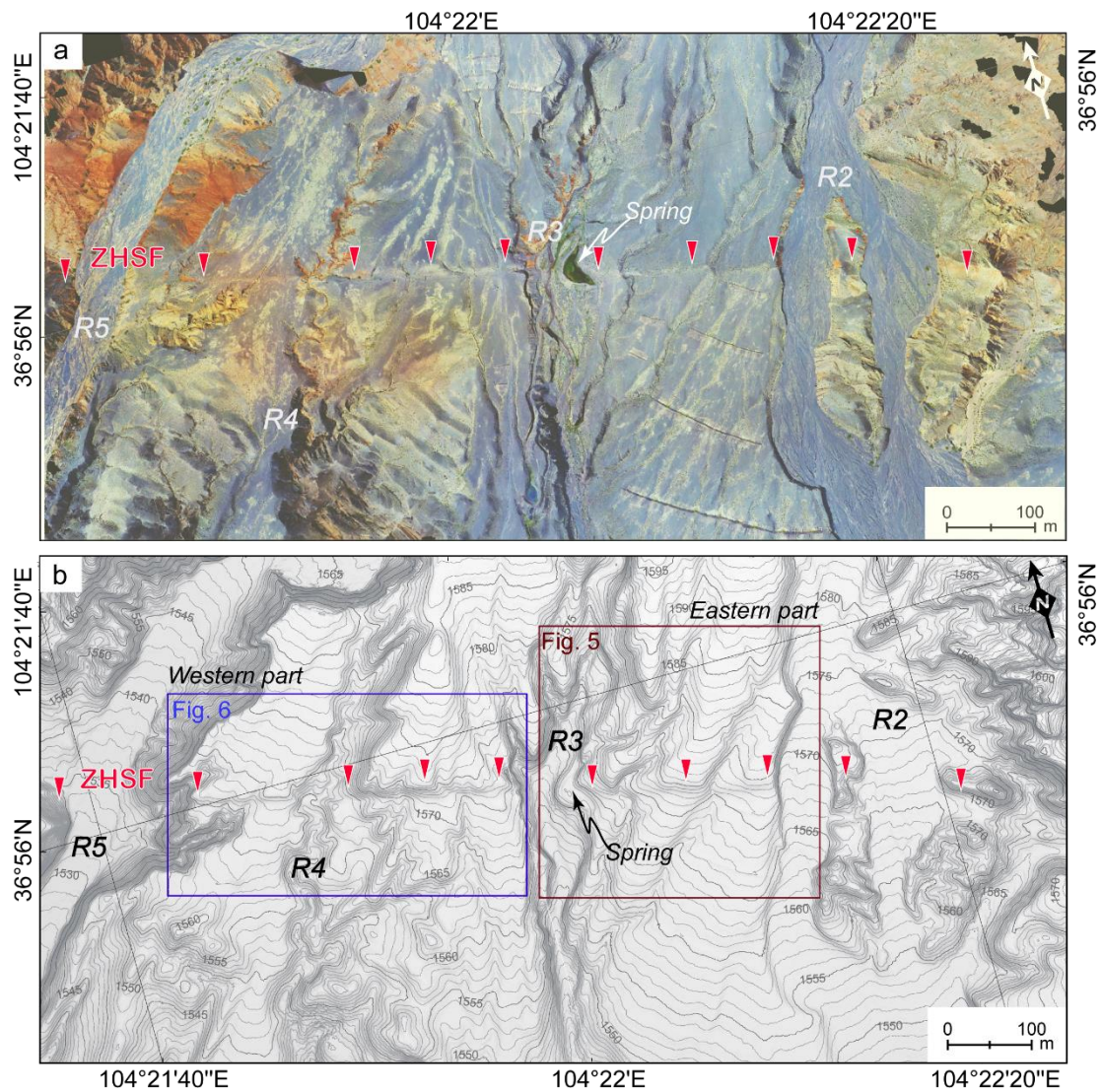
Note. Letters refer to piercing points in Figure 5.

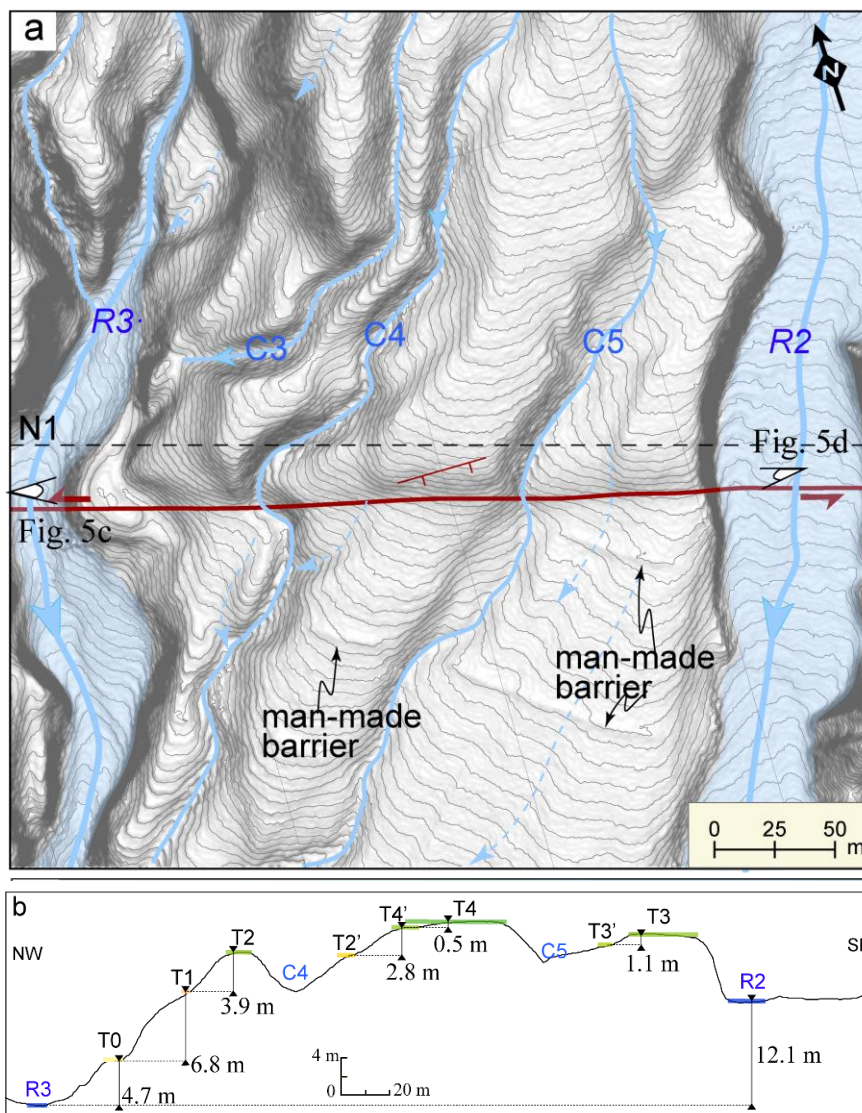


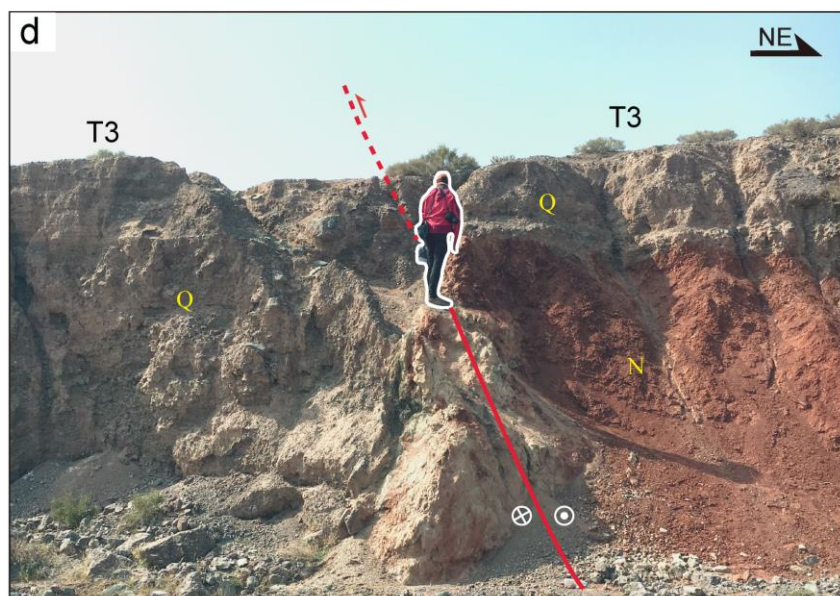
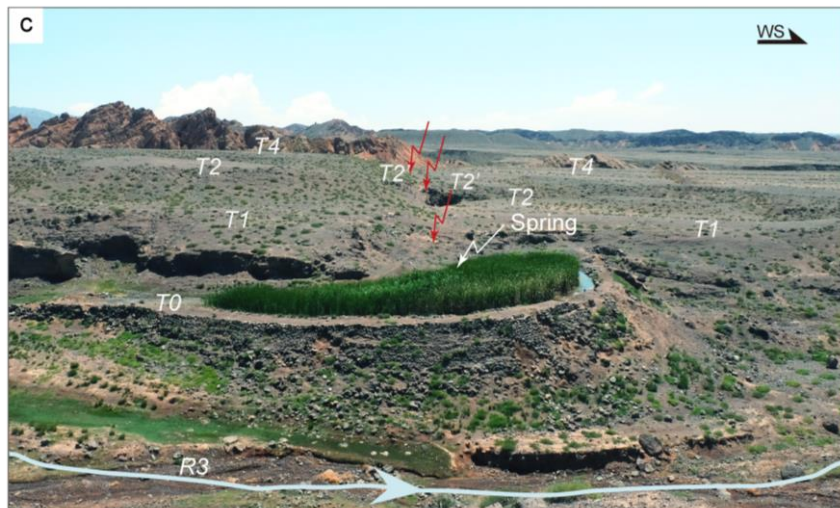


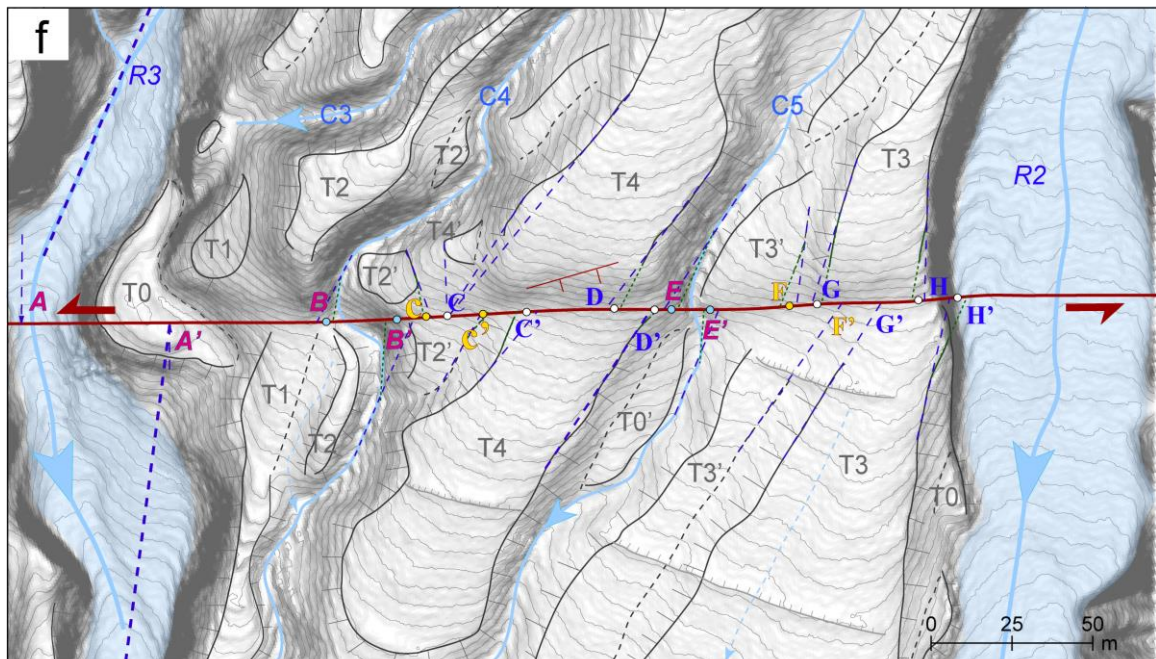
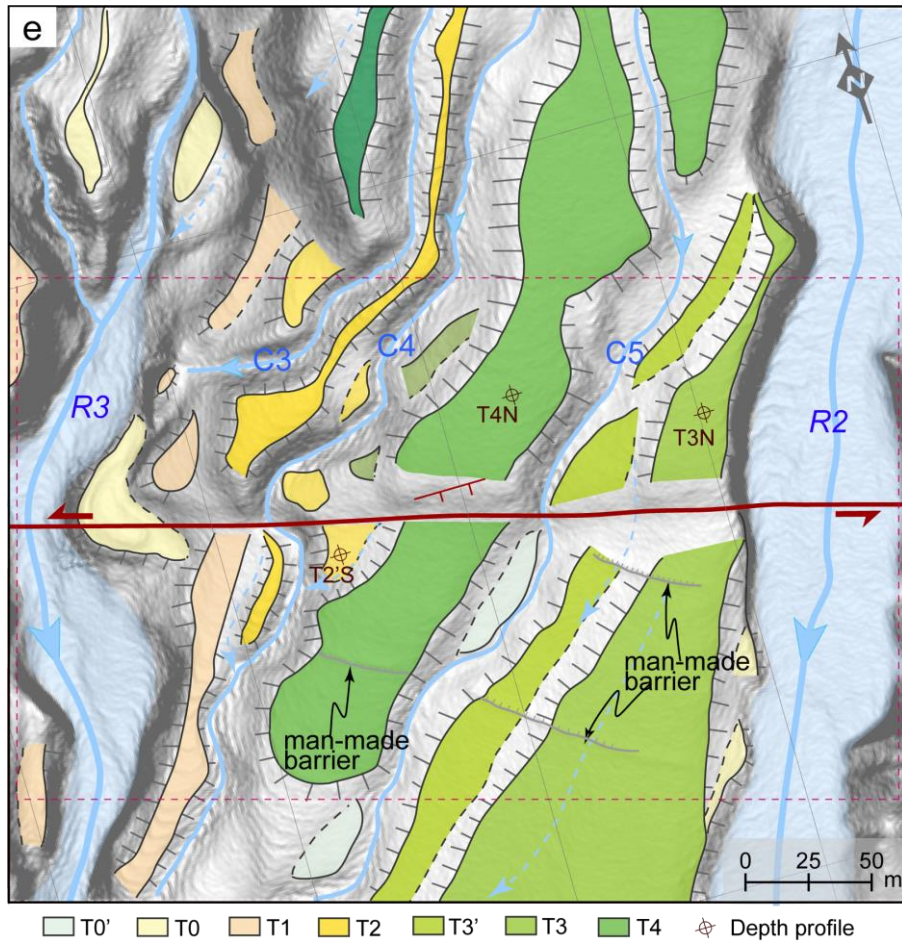


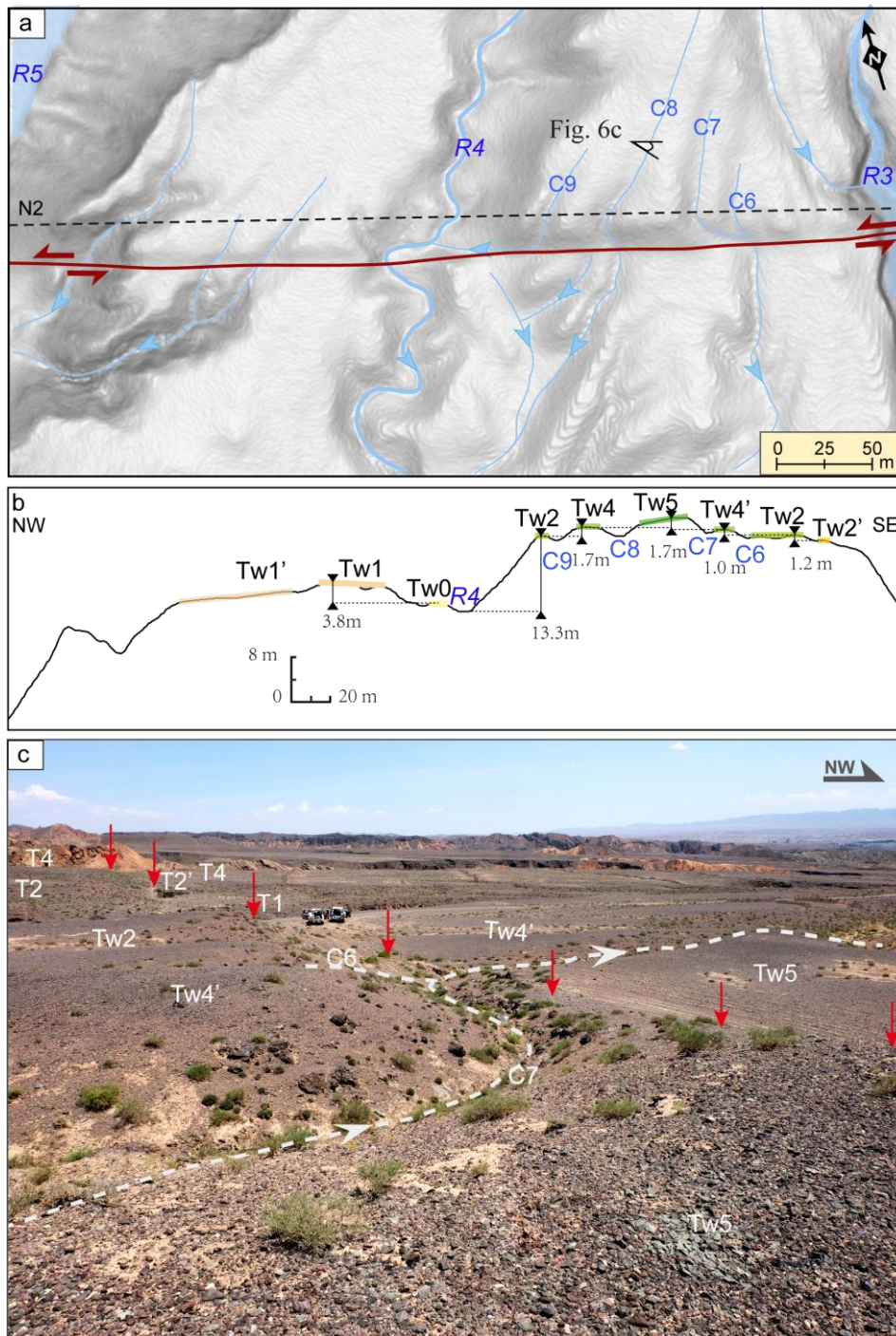


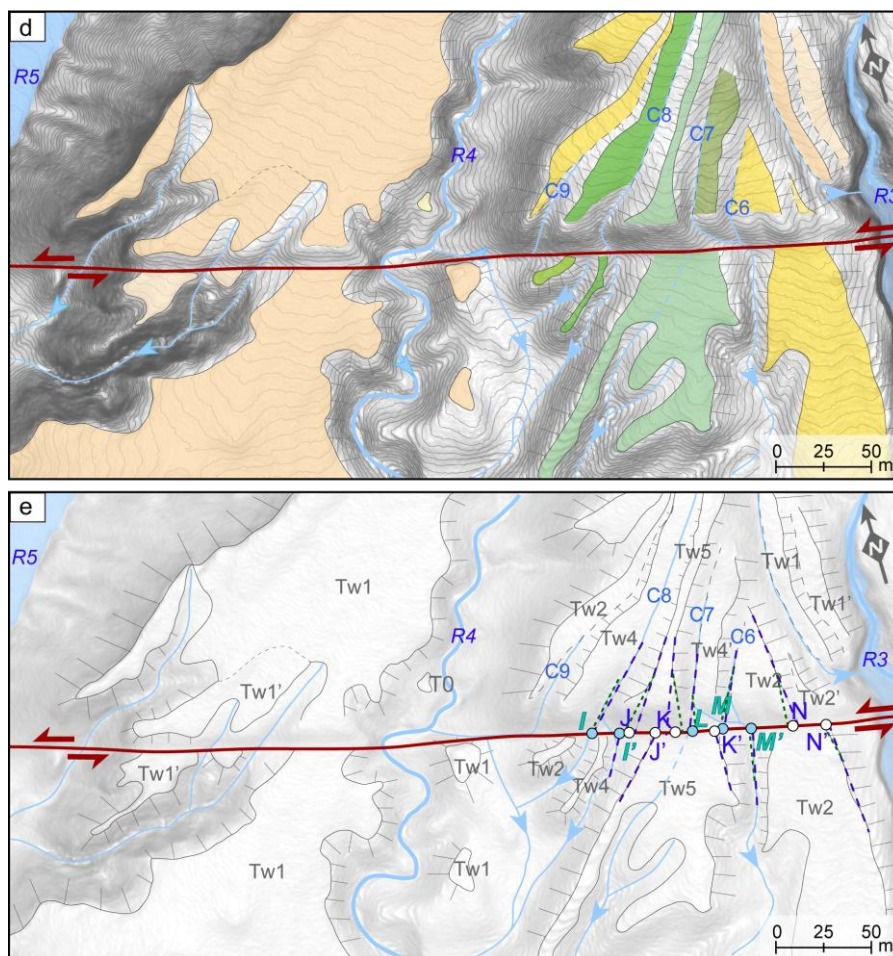


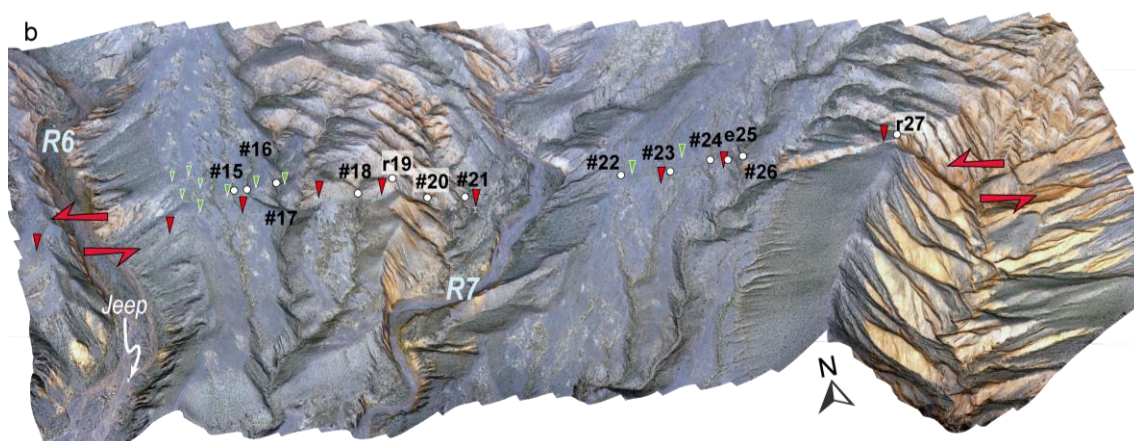
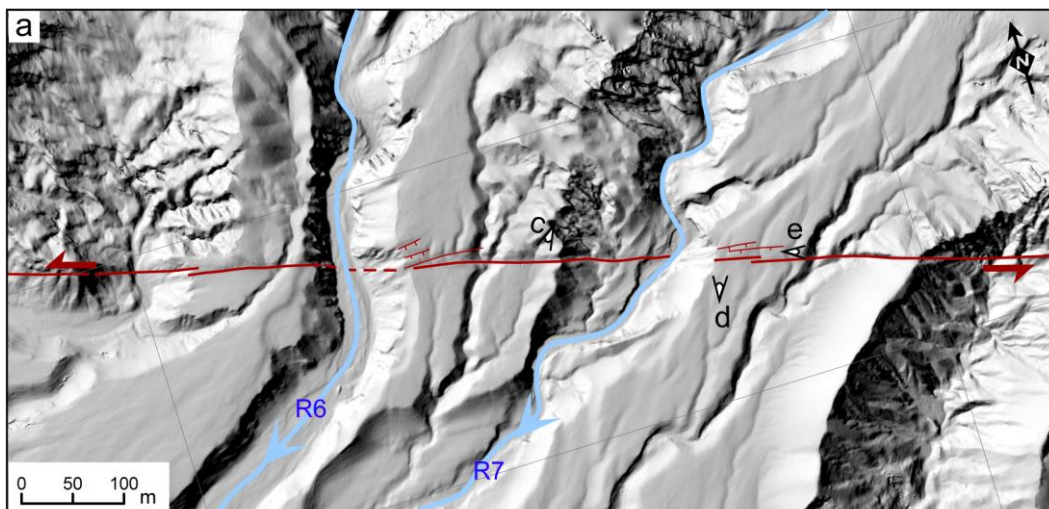












▽ main fault indicator ▼ secondary fault indicator
 #15 offset channel r19 offset ridge e25 offset terrace edge



